

1

2       **Unsteady Land-Sea Breeze Circulations in the Presence of a Synoptic Pressure Forcing**  
3       **Mohammad Allouche<sup>1,2</sup>, Elie Bou-Zeid<sup>1\*</sup>, and Juho Iipponen<sup>3</sup>**

4       <sup>1</sup>Department of Civil and Environmental Engineering, Princeton University, New Jersey

5       <sup>2</sup>Lawrence Livermore National Laboratory, Livermore, California

6       <sup>3</sup>Program in Atmospheric and Oceanic Sciences, Princeton University, New Jersey

7       \*Corresponding author: Elie Bou-Zeid ([ebouzeid@princeton.edu](mailto:ebouzeid@princeton.edu))

8       **Key Points:**

- 9       • Unsteady large-eddy simulations of land-sea breezes reveal asymmetric dynamics  
10       when the geostrophic wind is oriented from sea to land, versus land to sea.
- 11       • The diurnal dynamics result in non-equilibrium flows , and the sea patch is found  
12       to control the final turbulence-mean flow equilibrium response.
- 13       • An autonomous clustering, to delineate these macro circulations into four regimes  
14       (canonical, transitional, shallow land-driven, and advected), is successfully tested.

## 15 **Abstract**

16 Unsteady land-sea breezes (LSBs) resulting from time-varying surface thermal contrasts  
 17  $\Delta\theta(t)$  are explored in the presence of a constant synoptic pressure forcing,  $M_g$ , when the  
 18 latter is oriented from sea to land ( $\alpha=0^\circ$ ), versus land to sea ( $\alpha=180^\circ$ ). Large eddy  
 19 simulations reveal the development of four distinctive regimes depending on the joint  
 20 interaction between  $(M_g, \alpha)$  and  $\Delta\theta(t)$  in modulating the fine-scale dynamics. Time lags,  
 21 computed as the shifts that maximize correlation coefficients of the dynamics between  
 22 transient and the corresponding steady state scenarios at  $\Delta\theta=\Delta\theta_{\max}$ , are found to be  
 23 significant and to extend 2 hours longer for  $\alpha=0^\circ$  compared to  $\alpha=180^\circ$ . These diurnal  
 24 dynamics result in non-equilibrium flows that behave differently over the two patches for  
 25 both  $\alpha$ 's. Turbulence is found to be out of equilibrium with the mean flow, and the mean  
 26 itself is found to be out of equilibrium with the thermal forcing. The sea surface heat flux  
 27 is consistently more sensitive than its land counterpart to the time-varying external  
 28 forcing  $\Delta\theta(t)$ , and more so for synoptic forcing from land-to-sea ( $\alpha=180^\circ$ ). Hence,  
 29 although the land reaches equilibrium faster, the sea patch is found to exert a stronger  
 30 control on the final turbulence-mean flow equilibrium response. Finally, vertical velocity  
 31 profile at the shore and shore-normal velocity transects at the first grid level are shown to  
 32 encode the multiscale regimes of the LSBs evolution, and can thus be used to identify  
 33 these regimes using  $k$ -means clustering.

## 34 **Plain Language Summary**

35 Advancing our understanding of atmospheric circulation dynamics in coastal regions is  
 36 essential as these zones host most of the world's population and economic activity. These  
 37 dynamics have an oversized influence on our ability to better predict pollution ventilation  
 38 and urban heat island induced-dynamics in coastal cities. In this study, we investigate the  
 39 diurnal cycles of land-sea breeze circulations, with the aid of a state of art numerical  
 40 simulation tool in the presence of increasingly large scale weather systems. These  
 41 simulations depict added complexities as the land-sea surface thermal contrasts, mean  
 42 flow, and turbulence are found to be consistently out of equilibrium. The gained physical  
 43 insights from this analysis offer new explanations on why coarse weather and climate  
 44 models inherently fail to reproduce such unresolved processes, but also offer a pathway  
 45 for better understanding and prediction. Specifically, an autonomous clustering approach

to independently classify these multiscale circulations is successfully tested against visual categorization, identifying four emerging regimes.

**Keywords:** Coastal zones, Land-sea breeze, Non-equilibrium turbulence, Thermal circulation, Unsteady atmospheric boundary layer

## 1 Introduction

Real-world land-sea breezes (LSBs) are perceptibly unsteady. Simulating such transient scenarios is thus motivated by the need to provide a more realistic picture of the evolution of winds within the coastal Atmospheric Boundary Layer (ABL), and how they respond to the interaction of the LSBs with a synoptic pressure forcing. This would be beneficial in many applications including (i) advancing our knowledge on the diurnal potential of offshore wind power where these LSBs might amplify or reduce the available power (Howland et al., 2020; Kumer et al., 2016; Porté-Agel et al., 2020), (ii) improving the forecast of pollutant dispersion (Levy et al., 2009; Llaguno-Munitxa & Bou-Zeid, 2018; Lyons, 1995), as well as rainfall and cloud formation (Mazon & Pino, 2015) in coastal regions; and (iii) characterizing the implications of LSBs on the environment and the microclimatic conditions of coastal cities (Bauer, 2020; Lin et al., 2008; Lo et al., 2006). In addition, from energy systems and design perspectives, forecasting the intermittent wind power is a key element to ensure a stable electricity grid, analyze wind turbine blades fatigue, and optimize hub height and wind farm layouts (Díaz & Guedes Soares, 2020).

Previous studies on the topic of transient land-sea breezes have used observations and simulations (Antonelli & Rotunno, 2007; Atkison, 1995; Cana et al., 2020; Porson et al., 2007; Rizza et al., 2015; Segal et al., 1997; Sills et al., 2011; Steyn, 2003; Yang, 1991) to identify a number of important parameters that control the dynamics. These include: (i) the transient difference  $\Delta\theta(t)$  between land surface temperature  $\theta_L$  and sea surface temperature  $\theta_s$  and its natural time scale (usually 24 hours), (ii) the speed ( $M_g$ ) and direction ( $\alpha$ ) of the synoptic pressure gradient forcing, (iii) the latitude as it influences the Coriolis parameter  $f$  and the associated time scale of inertial oscillations, (iv) land and sea roughness lengths for momentum and for heat, (v) land topography, and (vi) the height of the inversion and its strength. This vast parameter space prompted the authors of this

76 study to propose a reduction to a set of non-dimensional parameters (Allouche, Bou-Zeid,  
77 et al., 2023) to facilitate generalization of the physical findings and to guide numerical  
78 and experimental studies. In that prequel paper, we focused on analyzing the competing  
79 effects of synoptic forcing and thermal contrast under steady state conditions, identifying  
80 several distinct regimes of the LSBs and notable asymmetry in the synoptic effect when  
81 the geostrophic wind blew from land-to-sea or vice versa. The important transient effects  
82 were not considered, but they are the focus of the present study.

83 Previous similar studies on the topic of transient land-sea breezes used two-dimensional  
84 numerical models and compared to laboratory experiments. Sha et al., 1991 investigated  
85 how the Kelvin-Helmholtz (KH) instability affects the diurnal structures of these LSBs  
86 under light wind conditions. Similarly, Yoshikado, (1992) examined the basic  
87 characteristics of the daytime heat-island circulation and its interaction with the sea  
88 breeze and concluded that the urban heat-island effect could delay the inland transport of  
89 urban pollutants and potentially prevent their dispersion. Using a three-dimensional cloud  
90 resolving model, Dailey and Fovell (1999) explored how the horizontal convective rolls  
91 (HCRs) can modulate the convection process along the presence of sea-breezes (SBs)  
92 along  $\alpha=0^\circ$ . Similarly, Fovell and Dailey (2001) examined again the overall convective  
93 activity, with an alongshore ambient flow this time ( $\alpha=90^\circ$ ). Jiang et al., (2017) studied,  
94 using large-eddy simulation, how the streaky turbulent structures modulate SB front  
95 characteristics over urban-like coasts under strong wind shear and moderate buoyancy  
96 i.e., rendering the SB front into three-dimensional structures with strengthened updrafts.  
97 Also, Fu et al., (2021), with the aid of large-eddy simulation, explored over a peninsula  
98 the different generations of deep-convection initiation through the collision of two sea-  
99 breeze fronts. They reported how a decreased land heat flux weakens each of the  
100 identified generation until one reaches shallow convection. Others conducted laboratory  
101 experiments to analyze flow patterns associated with the land and sea breezes (Mitsumoto  
102 et al., 1983; Moroni & Cenedese, 2015; van der Wiel et al., 2017).

103 The enormous differences in heat capacity and available energy partitioning to latent heat  
104 between the sea (large) and land (small) explain why water surface temperature changes  
105 reduce to near-zero during a diurnal cycle. In contrast, land surface warms and cools  
106 more intensely due to its lower thermal conductivity and heat capacity (and thus lower

thermal admittance or effusivity), as well as higher Bowen ratio. Consequently, local meteorology is here largely controlled by the diurnal cycle of land surface temperature, along with the synoptic scale forcing. When synoptic pressure forcings are added, they induce a broad range of spatial transitions in buoyancy fluxes, jointly modulating these LSBs with the thermal contrast. One expected feature of such circulations is non-equilibrium turbulence exhibited as a hysteretic response of the surface kinematic fluxes, mean flow, and turbulence relative to the imposed forcing. Since most geophysical parameterizations still assume turbulence-mean equilibrium (Bou-Zeid et al., 2020a; Huang et al., 2013; Mahrt & Bou-Zeid, 2020), non-equilibrium could offer a partial explanation as to why climate models are still showing consistent upwelling biases (Lembo et al., 2019; Richter-Menge et al., 2017) (in addition to the systematic winds biases that are also attributed to the disparate resolutions of the atmospheric and oceanic grids. Therefore, an analysis with a prescribed land surface temperature pattern that reflects a canonical diurnal variation would offer new insights into the non-linear interplay between various mechanisms that evolve at different time scales and rates including (i) the inherent thermal and kinetic inertia (memory) effects of the air, (ii) the evolution of turbulent structures associated with the diurnal land surface forcing (Salesky et al., 2017), (iii) sea breeze (SB) and land breeze (LB) tendency for initiation, (iv) the strength of the advected inflows and their inherent asymmetric nature depending on the angle  $\alpha$  between the shore and geostrophic wind.

In this paper, we consider the same numerical setup introduced in (Allouche, Bou-Zeid, et al., 2023) for steady thermal contrasts, but here we account for the transient diurnal cycle of the surface temperature contrasts between land and sea  $\Delta\theta(t) = \theta_L(t) - \theta_S$ . As the expression suggests, we impose a constant sea surface temperature ( $\theta_S$ ) and a time-varying land surface temperature ( $\theta_L(t)$ ), while also including a constant synoptic pressure forcing. We are thus able to compare the unsteady simulations we conduct here to the reference steady state scenarios we reported before (Allouche, Bou-Zeid, et al., 2023), hereafter referred to by ABI23, where the surface thermal contrast is fixed at  $\Delta\theta = 10$  K. Specifically, we aim to answer the following questions: (Q1) How do the joint interaction between the synoptic variables ( $M_g$ ,  $\alpha$ ) and transient surface thermal contrasts  $\Delta\theta(t)$  modulate the fine-scale dynamics and structures of the LSBs? The complexity of

the emergent circulations and the disparate flow features over the two patches motivate the second question: (Q2) How do the surface kinematic fluxes, shoreline mass exchanges, and turbulence evolve with the external parameters ( $M_g$ ,  $\alpha$ ) and  $\Delta\theta(t)$  and is there hysteresis? Finally, visual identification of the circulation regimes motivates the last question: (Q3) What are the best criteria to autonomously delineate the emerging LSBs from a macro (large scale) and micro (near surface) perspectives?

In section 2, an expanded dimensional analysis, based on the one outlined in ABI23, is presented. In section 3, the numerical experiments design (boundary and initial conditions) is detailed. The thermal circulation flow structures are then discerned and visually categorized in sections 4 and 5 (answering Q1). In section 6, land and sea surface kinematic fluxes, shoreline exchanges, and turbulence are investigated (answering Q2). In section 7, criteria are proposed to demarcate these LSBs from a macro and micro categorization (answering Q3). Finally, conclusions and implications of this work are drawn in section 8.

## 2 Dimensional analysis

This section builds on the dimensional analysis outlined by ABI23, where a set of dimensionless groups was constructed based on Buckingham's Pi theorem for the steady state dynamics where that theorem applies. The pertinent dimensional external input parameters to our problem involve three length scales: (i)  $z_{0,L} = 0.002$  (m), the land surface roughness length, (ii)  $z_{0,S} = 0.002$  (m), the sea surface roughness length (here not a function of wind), and (iii)  $z_i = 1600$  (m), the ABL height. The thermal roughness lengths are assumed to be fully determined by, but not necessarily equal to, their momentum counterparts. In addition, two velocity scales are of relevance: (i)  $M_g = [U_g^2 + V_g^2]^{1/2}$  the geostrophic wind magnitude, and (ii)  $W_*(t) = [g\beta z_i(\Delta\theta(t))]^{1/2}$ , a time varying convective buoyant velocity scale where  $g = 9.81$  ( $\text{m s}^{-2}$ ) is the gravitational acceleration,  $\beta = 1/\theta_r$  ( $\text{K}^{-1}$ ) the volumetric expansion coefficient of air,  $\theta_r = 300$  (K) a reference temperature in the Boussinesq approximation sense, and  $\Delta\theta(t) = \theta_L(t) - \theta_S$  (K), (refer to Fig. 1, top).

166 For unsteady state analysis, the flow physics are also influenced by two time scales  
 167 arising from (i)  $2\pi/f_c \approx 12.5$  h, the inertial period, where  $f_c = 1.394 \times 10^{-4}$  Hz is the Coriolis  
 168 parameter (at lower latitudes, this time scale is much longer and less important, reflecting  
 169 the waning influence of the Coriolis force), and (ii)  $2\pi/\omega = 24$  h, the diurnal earth surface  
 170 heating/cooling rate (corresponding to the variability in buoyancy forcing,  $\tau_{forcing} = 24$  h),  
 171 shown later to dominate the transient dynamics. The kinetic and thermal inertia times  
 172 scales will also modulate the response. These time scales will depend on the problem  
 173 setup, as well as on the extent of the thermal circulation, but should be much shorter than  
 174 12.5 or 24 h. We will revisit these scales when we discuss the hysteresis of the dynamics.  
 175 Finally, the alignment angle  $\alpha$  between the shore and the geostrophic velocity vector is  
 176 the only non-dimensional variable that forms one of the dimensionless groups. Therefore,  
 177 any output of the numerical experiments, with  $n=8$  input dimensional parameters and  $k=2$   
 178 independent dimensions (L, T), can be also non-dimensionalized and expressed in terms  
 179 of  $n-k=6$  dimensionless groups. The five identified  $\Pi$ 's by ABI23, some of which are  
 180 here variable in time, are stated here for reference: two dimensionless parameters are  
 181 related to the introduced length scales  $\Pi_1 = z_{0,L}/z_{0,S}$  (surface roughness contrast expressed  
 182 as inner scales ratio) and  $\Pi_2 = z_i/z_{0,S}$  (outer to inner scales ratio, commensurate with a  
 183 Reynolds number of the problem). Another dimensionless group is associated with the  
 184 velocity scales  $\Pi_3(t) = Ri^{-1}(t) = M_g^2/[g\beta z_i(\theta_L(t) - \theta_S)] = M_g^2/W_*(t)^2$ , which is an inverse  
 185 bulk Richardson number that relates inertia to buoyancy. An inverse convective Rossby  
 186 number also arises, comparing the convective/buoyant and inertial time scales  
 187  $\Pi_4(t) = (z_i/W_*(t))/(2\pi/f_c)$ , and  $\Pi_5 = \alpha$ . The last new emerging number, resulting from the  
 188 aforementioned two time scales ( $2\pi/f_c \approx 12.5$  h and  $\tau_{forcing} = 24$  h), is  $\Pi_6 = 2\pi/f_c / \tau_{forcing}$   
 189  $\approx 0.52$ . The time evolution can then also be described as a function of the non-  
 190 dimensional time  $\omega t$ . The time variability of the problem precludes exact applicability of  
 191 the Buckingham Pi theorem, and thus exact similarity. But the non-dimensionalization  
 192 remains an effective tool for reducing the parameter space and elucidating the physics.

193 In this paper, the simulations consider only the effects of the synoptic variables  $M_g$  (m/s),  
 194 which here takes on the value 0, 0.4, 1.2 and  $2 \text{ ms}^{-1}$ ,  $\alpha = 0^\circ$  or  $180^\circ$ ), and  $\Delta\theta(t) = \theta_L(t) -$

195  $\theta_s$ .  $\Pi_1$  is set to 1 to isolate the impact of the thermal torque (due to temperature  
 196 differences) from that of the stress torque (that is mainly controlled by roughness  
 197 differences) (Bou-Zeid et al., 2020b). In addition,  $\Pi_2 = 8 \times 10^5$  is fixed to a high value  
 198 ensuring a high Reynolds number and large separation of turbulent to friction scales. The  
 199 convective Rossby number  $\Pi_4$  must vary in time since it is a function of the thermal  
 200 contrast.

### 201 **3 Large eddy simulations**

#### 202 *3.1 Governing equations*

203 As described by ABI23, the used LES code solves the spatially filtered incompressible  
 204 mass continuity and Navier-Stokes momentum equations using the Boussinesq  
 205 approximation for the mean state, in addition to the advection-diffusion equation for the  
 206 potential temperature, which are given respectively as follows:

$$\frac{\partial \tilde{u}_i}{\partial x_i} = 0, \quad (1)$$

$$\frac{\partial \tilde{u}_i}{\partial t} + \tilde{u}_j \left( \frac{\partial \tilde{u}_i}{\partial x_j} - \frac{\partial \tilde{u}_j}{\partial x_i} \right) = -\frac{1}{\rho} \frac{\partial \tilde{p}^*}{\partial x_i} - \frac{\partial \tau_{ij}}{\partial x_j} - g \frac{\tilde{\theta}'}{\theta_r} \delta_{i3} + f_c (U_g - \tilde{u}_1) \delta_{i2} - f_c (V_g - \tilde{u}_2) \delta_{i1}, \quad (2)$$

$$\frac{\partial \tilde{\theta}}{\partial t} + \tilde{u}_j \frac{\partial \tilde{\theta}}{\partial x_j} = -\frac{\partial \pi_j}{\partial x_j}. \quad (3)$$

207 The tilde ( $\sim$ ) represents filtered quantities (omitted throughout the rest of paper for  
 208 simplicity since we only deal with filtered LES outputs);  $x_i$  (or  $X_i$ ) is the position vector;  
 209  $\tilde{u}_i$  (or  $U_i$ ) is the resolved velocity vector (the indices  $i$  and  $j$  span the three directions 1 for  
 210  $X$  (across shore), 2 for  $Y$  (along shore), and 3 for  $Z$  (vertical));  $t$  is time;  $\rho$  is the density of  
 211 air;  $p^*$  is a modified perturbation pressure that includes the resolved and unresolved  
 212 turbulent kinetic energy;  $\tau_{ij}$  is the anisotropic part of the full sub-grid scale (SGS) stress  
 213 tensor  $\sigma_{ij} = \tilde{u}_i \tilde{u}_j - \tilde{u}_i \tilde{u}_j$ ;  $\theta$  is the potential temperature with its reference value  $\theta_r$ ;  $\theta'$  is  
 214 the deviation of the local  $\theta$  from its horizontal planar average in the LES;  $\delta_{ij}$  is  
 215 the Kronecker delta; and  $\pi_j = \tilde{\theta} \tilde{u}_j - \tilde{\theta} \tilde{u}_j$  is the SGS heat flux vector. The prime always  
 216 denotes the turbulent perturbation from a mean state, indicated by an overbar. The SGS



217 stress and heat flux are parameterized using a scale-dependent Lagrangian dynamic  
 218 model that was extensively validated (Bou-Zeid et al., 2005; Huang & Bou-Zeid, 2013;  
 219 Kumar et al., 2006), with a constant SGS Prandtl number of 0.4. The computational grid  
 220 is a uniform structured mesh, staggered in the vertical direction to compute vertical  
 221 derivatives using second-order centred differences. Horizontal derivatives are computed  
 222 spectrally, and thus the domain must be periodic in the horizontal directions, but we  
 223 modify it to impose inflow in the  $X$  direction, as clarified in subsection 3.3. An Adams-  
 224 Bashforth second-order explicit time advancement scheme is used.

### 225 3.2 Suite of simulations

226 The designed simulations, illustrated in Fig. 2, span seven cases, one case for  $M_g=0$  and  
 227 six cases with all combinations of  $\{M_g$  (m/s): 0.4, 1.2, 2 and  $\alpha$ :  $0^\circ$ ,  $180^\circ\}$ . The domain  
 228 size is  $L_x = 80 \text{ km} \times L_y = 5 \text{ km} \times L_z = z_i = 1.6 \text{ km}$ . The corresponding baseline number of  
 229 grid points ( $N_x, N_y, N_z$ ) is  $384 \times 24 \times 64$ . The grid resolution ( $dX = dY = 208 \text{ m}$ ,  $dZ = 25 \text{ m}$ )  
 230 is course relative to typical ABL LES studies, and the simulations thus represent a very  
 231 large eddy simulation of the problem, where a significant fraction of the production range  
 232 may not be resolved (Pope, 2001), but the analyses focus primarily on the mean flow and  
 233 secondary circulations that are well resolved.

### 234 3.3 Boundary and initial conditions

235 For both scenarios (null or positive  $M_g$ ), the boundary conditions are set periodic in the  $Y$   
 236 direction for velocities and temperature in all simulations to mimic an infinite coastline.  
 237 A stress-free impermeable lid boundary condition at top of the domain is imposed for the  
 238 velocities because any resultant LSB might be sensitive to the free tropospheric profiles  
 239 and inversion strength (Cioni & Hohenegger, 2018), and in this paper we want to avoid  
 240 adding yet another parameter to the investigation (our setup thus mimics a very strong  
 241 inversion). The surface temperatures of the two patches are imposed as  $\theta_s = 278.15 \text{ K}$  and  
 242  $(\theta_L(t) = \theta_s + \Delta\theta_{max} \sin(\omega t))$ , where  $\Delta\theta_{max} = \theta_{L,max} - \theta_s = 10 \text{ K}$ ,  $t$  in hours), and surface  
 243 stresses and heat fluxes are calculated using a local equilibrium wall-model based on a  
 244 log-law with Monin-Obukhov stability correction (Bou-Zeid et al., 2005; Ghannam &  
 245 Bou-Zeid, 2021).

As sketched in Fig. 2 of ABI23, two equal buffer regions on the streamwise boundaries of the domain are implemented with tangent hyperbolic interpolation to act as smooth transitions of the streamwise flow (since the numerical code is pseudo-spectral and periodic in  $X$ ) (Lund et al., 1998; Spalart, 1988), and realistic upstream inflows for a range of geostrophic wind conditions (for both  $\alpha$  values) are generated using precursor simulations. The length of the buffer area ( $L_{Buffer}$ ) on each side is 1/16 of  $L_x$  ( $\approx 5$  km). A region twice the buffer length on either side of the domain in  $X$  is excluded from analysis to further minimize the impact of streamwise boundary conditions. As described in ABI23, the  $X$  boundary conditions are treated differently when (i)  $M_g=0$ : no-slip boundary condition (NS-BC:  $U=V=W=0$ ) or (ii)  $M_g \neq 0$ : the inflows for velocities and temperature are generated in precursor simulations with periodic boundary conditions in both  $X$  and  $Y$  directions.

The imposed surface temperature (and thermal roughness lengths) in the precursor simulations is set equal to the value of the sea ( $\theta_s = \text{constant temperature}$ ) when  $\alpha=0^\circ$  or land ( $\theta_L(t) = \text{time varying temperature}$ ) when  $\alpha=180^\circ$  to represent an infinitely homogeneous upstream fetch. The nature of these generated inflows is thus drastically different for the two considered directions. As demonstrated in the bottom panel of Fig. 1, for  $\alpha=180^\circ$ , transiently saved inflows, which mimic the continuous evolution of structures in response to the same sinusoidal diurnal land surface temperature profile, are fed at the same physical time in the heterogeneous simulation. Therefore, such inflows inherently span a wide range of stabilities. On the other hand, for  $\alpha=0^\circ$ , the generated inflows mimic an infinite persistently near-neutral sea. In this case, the saved inflows are only needed over the last quarter inertial period ( $0.25 \times \tau_f = 3.125$  h) out of the total sea precursor simulations time ( $T = 4.25 \times \tau_f = 53.125$  h), and these inflows are recycled every  $0.25 \times \tau_f$  in the  $\alpha=0^\circ$  main simulations. Since the internal dynamics of the main domain are evolving, this recycling will not produce identical flows repeated every  $0.25 \times \tau_f$  in the main domain.

In all the simulated scenarios in this paper, the initial air temperature in the whole analysis domain is uniformly set equal to the sea surface temperature ( $\theta_{init} = \theta_s = 278.15$  K).

275 Similarly, the land surface temperature is initiated with  $\theta_L(t_0) = \theta_S = 278.15$  K. All  
 276 analyzed statistics here (null and finite synoptic forcing) refer to the third diurnal cycle,  
 277 i.e., the 24-hour period that follows the initial 48-hour simulation spin up, as illustrated in  
 278 Fig. 1, bottom panel. The same synoptic pressure gradient (as a geostrophic wind) used to  
 279 generate the inflow is imposed as well in the main simulation domain, and thus we do not  
 280 rely solely on the inflow inertia to represent the synoptic flow. A schematic diagram of  
 281 the three-dimensional domain and the boundary conditions is given in Fig. 2.

#### 282 **4 Thermal circulation structures: Snapshot dynamics at selected times**

283 The features of the simulated transient LSBs, and how they are jointly modulated by ( $M_g$ ,  
 284  $\alpha$ ) and  $\Delta\theta(t) = \theta_L(t) - \theta_S$ , are explored in this section. Figs. 3 and 4 depict pseudocolor  
 285 plots of the along-shore and time averaged stream-wise  $\langle U \rangle_{y,t}$  (brackets will henceforth  
 286 denote averaging along-shore in  $y$  and in time over 1 hour centered around the  $\Delta\theta(t)$   
 287 reported in the figure or analysis) through an  $X$ - $Z$  slice of the analysis domain [ $X=10$  km-  
 288 70 km] (twice the buffer zone is excluded). The series of column panels in each figure  
 289 correspond to the same  $\alpha$  with increasing  $M_g$ , and the series of row panels in each figure  
 290 correspond to the same ( $M_g$ ,  $\alpha$ ) at different times and thus different contrasts  $\Delta\theta(t)$   
 291 (subscript 1: corresponds to quarter-periods prior to  $\Delta\theta=\Delta\theta_{max}$  and  $\Delta\theta=\Delta\theta_{min}$ , and  
 292 subscript 2: corresponds to quarter periods following  $\Delta\theta=\Delta\theta_{max}$  and  $\Delta\theta=\Delta\theta_{min}$ ). The  
 293 selected color bar ranges for  $\langle U \rangle_{y,t}$  (m/s) are kept unchanged in all figures to provide a  
 294 basis for a clear comparison. Pseudocolor plot movies of  $\langle U \rangle_{y,t}$  and  $\langle \theta \rangle_{y,t}$  are also  
 295 generated for these scenarios (see movies through the links provided in section 5). First  
 296 and as depicted in these figures, the four regimes that emerge will be introduced and  
 297 briefly in the following subsections, regime 1: canonical LSBs (subsections 4.1.1:  
 298 canonical SB and 4.1.2: canonical LB), regime 2: transitional LSBs (subsection 4.2),  
 299 regime 3: land-driven SB (subsection 4.3), and regime 4: advected LSBs (subsection 4.4).  
 300 Second, an overview of the transient behavior in all scenarios with respect to  $\Delta\theta(t)$  is  
 301 discussed afterwards, in section 5.

#### 302 4.1 Canonical LSBs

303 With a weak or zero  $M_g$ , a canonical counterclockwise deep thermal circulation  
 304 (canonical SB) is established because of the positive thermal contrast between the colder  
 305 sea (left patch) and the warmer daytime land (right patch) when  $\Delta\theta > 0$ . When the sign of  
 306 this thermal contrast is reversed ( $\Delta\theta < 0$ ) for the same setup scenario, the resultant steady  
 307 state LSB is just a mirror image of the original canonical SB; that is, another canonical  
 308 clockwise deep thermal circulation (canonical LB) would form.

309 The canonical sea breeze can be noted in the subplots corresponding to  $M_g=0$  at  $\Delta\theta_1=5$ ,  
 310  $\Delta\theta=10$ ,  $\Delta\theta_2=5$ ,  $\Delta\theta_2=0$  and  $\Delta\theta_1=-5$ ) in Fig. 3. Such regime is featured also for both  
 311 directions  $\alpha=0^\circ$  and  $180^\circ$ , but more consistently for  $\alpha=0^\circ$ , in the subplots that correspond  
 312 to  $\alpha=0^\circ$ ,  $M_g=0.4$  and  $1.2$ :  $\Delta\theta_2=5$ ,  $\Delta\theta_2=0$  and  $\Delta\theta_1=-5$  of Fig. 3 and  $\alpha=180^\circ$  with  $M_g=0.4$   
 313 only and for  $\Delta\theta_2=5$ ,  $\Delta\theta_2=0$  of Fig. 4. Canonical land breeze, on the other hand, is shown  
 314 in the subplot ( $M_g=0$ ,  $\Delta\theta_2=-5$ ), and it prevails upon continuing the cycle in the subplot  
 315 ( $M_g=0$ ,  $\Delta\theta_1=0$ ). Canonical land breeze LSBs exist also along both directions in the  
 316 subplots that correspond to ( $\alpha=0^\circ$  and  $180^\circ$ ,  $M_g=0.4$ ,  $\Delta\theta=-10$ ) of Figs. 3 and 4.

#### 317 4.2 Transitional thermal circulation

318 When the LSB is shifting regimes between the clear canonical reference states, we  
 319 observe a transitional state with no definite pattern; e.g., refer to the initiation of land  
 320 breeze in the lower ABL with a canonical SB background in the subplot  $\{M_g=0$ ,  
 321  $\Delta\theta_1=-10\}$  in Fig. 3. One can recognize here three circulation cells because of the created  
 322 entrainment zones. Such regimes generally inherit remnants of clearly categorized  
 323 circulations (reference states), but acquire features of an emerging regime that slowly  
 324 develops over time. When the synoptic wind blows from sea to land ( $\alpha=0^\circ$ ) or land to sea  
 325 ( $\alpha=180^\circ$ ) at  $M_g=0.4$ , as depicted in Figs. 3 and 4, the three corresponding subplots in each  
 326 figure ( $M_g=0.4$ :  $\Delta\theta_1=0$ ,  $\Delta\theta_1=5$ ,  $\Delta\theta=10$ ) all belong to the transitional LSB regime.  
 327 However, when the land is about to start cooling, only the advanced cooling subplot of  
 328 Fig. 3 ( $\alpha=0^\circ$ ,  $M_g=0.4$ :  $\Delta\theta_2=-5$ ) and the subplots of Fig. 4 ( $\alpha=180^\circ$ ,  $M_g=0.4$ :  $\Delta\theta_2=0$ ,  
 329  $\Delta\theta_1=-5$ ,  $\Delta\theta_2=-5$ ) qualify as transitional LSBs. In a nutshell, such a regime only exists at  
 330 weak synoptic forcings, i.e. for  $M_g \leq 0.4$ , and it is featured in both directions ( $\alpha=0^\circ$  and

180°) but at different times throughout the day since it depends on the strength and sign of the thermal contrast  $\Delta\theta(t)$ .

### 4.3 Land-driven thermal circulation

A different regime arises when the synoptic wind blows from land to sea ( $\alpha=180^\circ$ ), the land-driven LSB, as identified in ABI23. This regime features the development of a shallow persistent SB only along this direction ( $\alpha=180^\circ$ ), but this is conditioned on the strength of the pressure forcing  $M_g$  and  $\Delta\theta(t)$ . One remark here is that the transient dynamics feature this regime at  $M_g=1.2$  and 2 m/s only in the subplots corresponding to ( $\alpha=180^\circ$ :  $\Delta\theta=10$ ,  $\Delta\theta_2=5$ ,  $\Delta\theta_2=0$ ) of Fig. 4.

### 4.4 Advected thermal circulation

Advection LSBs display an almost unidirectional flow across the whole ABL domain; therefore, such flows do not feature any clear circulation cell, yet they might inherit some weak remnants of freshly eradicated LSBs. The flow in such regimes is nearly pressure driven, with almost no return air. This is clearly discerned along both directions, with the direction of the advected LSB dictated by  $\alpha$ . The subplots of Fig. 3 along ( $\alpha=0^\circ$ ,  $M_g=1.2$ :  $\Delta\theta_1=0$ ,  $\Delta\theta_1=5$ ,  $\Delta\theta=10$ ,  $\Delta\theta=-10$  and  $\Delta\theta_2=-5$ ) and ( $\alpha=0^\circ$ ,  $M_g=2$ : for all  $\Delta\theta$ ) demonstrate this regime i.e., “Advection-SL: from sea to land”. Similarly, the subplots of Fig. 4 ( $\alpha=180^\circ$ ,  $M_g=1.2$  and 2:  $\Delta\theta_1=0$ ,  $\Delta\theta_1=5$ ,  $\Delta\theta_1=-5$ ,  $\Delta\theta=-10$  and  $\Delta\theta_2=-5$ ) show this regime i.e., “Advection-LS: from land to sea this time”.

## 5 Thermal circulation structures: Evolving dynamics in time

Movies of the temperature and velocity field for both angles and selected geostrophic winds are available at the following links: they show the full 72 hours of simulations that include the warmup periods. Pseudocolor plot movies for the along shore, time averaged stream-wise velocity and temperature ( $\bar{U}_{y,t}$  and  $\bar{\theta}_{y,t}$ ) through an X-Z slice of the analysis domain were generated for  $M_g=0$  and for each  $\alpha$  ( $\alpha=0^\circ$  and  $\alpha=180^\circ$ ) in increasing  $M_g$  ( $M_g=0.4$ , 1.2 and 2 m/s). Overbar will henceforth denote along-shore averaging in  $Y$  and in time over 12.5 minutes prior to the time or  $\Delta\theta(t)$  indicated in the plots. The corresponding color bar ranges are the same ones used in generating Figs. 3 and 4.

- Temperature and velocity field at  $M_g = 0$  m/s

[https://www.dropbox.com/s/fbgfrsl7bqdmjp6/Mg0\\_mov\\_mixed1p\\_U\\_T%20Mohammad%20Allouche.mov?dl=0](https://www.dropbox.com/s/fbgfrsl7bqdmjp6/Mg0_mov_mixed1p_U_T%20Mohammad%20Allouche.mov?dl=0)

- Temperature field at  $\alpha = 0^\circ$ :

[https://www.dropbox.com/s/217xldri88j056/alpha0\\_mov\\_Mgs\\_1p\\_T%20Mohammad%20Allouche.mov?dl=0](https://www.dropbox.com/s/217xldri88j056/alpha0_mov_Mgs_1p_T%20Mohammad%20Allouche.mov?dl=0)

- Streamwise velocity field at  $\alpha = 0^\circ$ :

[https://www.dropbox.com/s/hou20d6skbpp287/alpha0\\_mov\\_Mgs\\_1p\\_U%20Mohammad%20Allouche.mov?dl=0](https://www.dropbox.com/s/hou20d6skbpp287/alpha0_mov_Mgs_1p_U%20Mohammad%20Allouche.mov?dl=0)

- Temperature field at  $\alpha = 180^\circ$ :

[https://www.dropbox.com/s/3qnkbt9takq4yn/alpha180\\_mov\\_Mgs\\_1p\\_T%20Mohammad%20Allouche.mov?dl=0](https://www.dropbox.com/s/3qnkbt9takq4yn/alpha180_mov_Mgs_1p_T%20Mohammad%20Allouche.mov?dl=0)

- Streamwise velocity field at  $\alpha = 180^\circ$ :

[https://www.dropbox.com/s/6n5uz17zo1wqqji/alpha180\\_mov\\_Mgs\\_1p\\_U%20Mohammad%20Allouche.mov?dl=0](https://www.dropbox.com/s/6n5uz17zo1wqqji/alpha180_mov_Mgs_1p_U%20Mohammad%20Allouche.mov?dl=0)

It is recommended to watch the movies before or while reading the rest of this section.

### 5.1 Transient LSBs along $M_g=0$

The subplot ( $M_g=0$ ,  $\Delta\theta_1=5$ ) in Fig. 3 depicts a canonical SB that is well established over the whole analysis domain. Further increase in the thermal contrast would favor two simultaneous mechanisms. First, the canonical SB is expected to intensify as buoyancy is enhanced, and second, the convective thermals would start to develop over land. The interaction between these newly born thermals and the SB is noticed in the  $\{M_g=0$ ,  $\Delta\theta=10\}$  subplot, but it is more discernable in the  $\{M_g=0$ ,  $\Delta\theta_2=5\}$  subplot where the matured convective rolls infiltrate through the already established SB and modify its onshore penetration distance. After that time, the weakening of buoyancy over land at  $\{M_g=0$ ,  $\Delta\theta_2=0\}$  causes the SB to reintensify rapidly and the thermals to lose structure, thus the SB's front pushes inland again. In the subplot  $\{M_g=0$ ,  $\Delta\theta_1=-5\}$ , and although the temperature contrast sign is reversed here, the SB's thermal and kinetic inertias cause it to continue to expand up to the end of the domain, rendering the land stable, and gaining its canonical shape again. The tendency here is for the land to become more stable as it

389 cools, and this is aided by the mildly stable background when  $\Delta\theta$  first becomes negative  
390 because of the SB penetration.

391 When  $\Delta\theta_1=-5$ , the existing SB has not been damped yet because suppressing its kinetic  
392 energy solely by buoyancy destruction (attributed to stable ABL due to nocturnal  
393 cooling) is a slower process (than its generation) due to the stable stratification over land  
394 that reduces friction and heat exchange (especially that here the land is kept relatively  
395 smooth, so mechanical production of turbulent kinetic energy is weak). Further reducing  
396 the surface thermal contrast favors the formation of a more intensified internal stable  
397 boundary layer over land. Thus, a significant negative surface  $\Delta\theta$  ( $\Delta\theta=-10$ ) induces land  
398 breeze initiation only near the surface, slowly expanding vertically, remaining shallow  
399 and below the previously established SB from the daytime, as depicted in the subplot  
400  $\{M_g=0, \Delta\theta=-10\}$ . Sustained colder land temperatures finally fully deplete the sea breeze,  
401 establishing a canonical land breeze later during the night, as shown in the subplot  
402  $\{M_g=0, \Delta\theta_2=-5\}$ .

403 Completing the cycle in the subplot  $\{M_g=0, \Delta\theta_1=0\}$  in the top row, the land breeze  
404 prevails before the land becomes warmer than the sea. As the cycle restarts and the land  
405 warms  $\{M_g=0, \Delta\theta_1=5\}$ , the bulk circulation reverses more rapidly than during the day-  
406 to-night transition. The cold air remaining from the nighttime over land delays the onset  
407 of thermal convection. Thus, the intrinsic LSB's thermal and kinetic memory effects  
408 delay the land stability response, and the development of convection does not start until  
409  $\Delta\theta=10$ , when the overlying LSB stable boundary layer is eradicated. Hence, one should  
410 be careful in analyzing LSBs as they are highly sensitive to the initial thermal and kinetic  
411 pervious states, especially under weak synoptic forcings background.

412 The top of Fig. 5 shows the correlation coefficient  $R(t)$  between the two dimensional ( $x$   
413 and  $z$ ) fields with the transient  $U(x,z)$  simulated here, and its corresponding steady state  
414 "SS" scenario we simulated in our previous work. As could be anticipated,  $R(t)$  increases  
415 with time, and one could anticipate that it should tend towards 1 as time approaches 6 h,  
416 the point where  $\theta_L=\theta_{max}$  "SS". However,  $R(t)$  reaches a local maximum of 0.85 earlier  
417 (when  $\Delta\theta_1 \approx 6.75$  K), plateaus, and then starts decreasing. Here,  $R(t)$  reaches a local  
418 minimum of 0.56 because of the SB interaction with the convective rolls (that are not

seen in the SS cases), plateaus, and then starts increasing again as the thermals decay.  $R(t)$  attains the global maximum of  $R_{\max}=0.97$  (almost one), around 7 hours following the SS time ( $\tau_{lag} \approx 7$  h), when  $\Delta\theta_I \approx -3.25$  K and the surface temperature contrast has already reversed. Afterwards, and as expected  $R(t)$  starts to decorrelate during night times ( $\Delta\theta(t) \ll 0$ ) where it reaches a global minimum of around  $-0.79$  corresponding to a canonical LB (mirror of a canonical SB).

The bottom of Fig. 5 shows the corresponding averaged enstrophy “a physical measure of the circulation strength” transient behavior  $\varepsilon(t)$  relative to the SS value corresponding to  $\theta_L=\theta_{\max}$ . At the corresponding time to  $\theta_L=\theta_{\max}$ , the transient averaged enstrophy comprises only around 16% of the SS value, and then starts ramping up as  $R(t)$  approaches  $R_{\max}$ . Remarkably, it can be clearly seen that enstrophy reaches the global maximum ( $\varepsilon_{\max}$  is almost twice the SS value) exactly at the same time ( $\tau_{lag}$ ) corresponding to  $R=R_{\max}$ , as indicated by the vertical magenta dotted line.

Fig. 6 shows three snapshots of the time averaged stream-wise  $\langle U \rangle_{y,t}$  for the SS case of  $\theta_L=\theta_{\max}$  (top), the TR case “TR: transient” at the time corresponding to  $\theta_L=\theta_{\max}$  (middle), and TR case at the time corresponding to  $R=R_{\max}$  (bottom). The bottom TR case clearly reflects the main SS features (top), but it developed with a  $\tau_{lag} \approx 7$  h relative to the SS time ( $\Delta\theta_I \approx -3.25$  K) with our prescribed time-varying land surface temperature (which is idealized and different from the real world where it would be controlled by the surface thermal inertia and energy budget).

## 5.2 Transient LSBs with synoptic forcing along $\alpha=0^\circ$

Here a sea-to-land pressure gradient is added, along with  $Y$ - $Z$  inflow slices of the dynamics and flow structures of an infinite neutral flow over sea. The subplot  $\{M_g=0.4, \Delta\theta_1=0\}$  in Fig. 3 demonstrates a transitional regime where traces of the night land breeze are still discerned especially near the surface. This is accompanied by an inherent stable boundary layer over land (away from the surface) and offshore (just near the shore where the LB prevails), and almost a neutral ABL over the sea (because of the advected inflows). As the land heats up, in the subplot ( $M_g=0.4, \Delta\theta_1=5$ ), mixing is more favored



447 over land and the unstable boundary layer near the surface deepens and weakens the  
448 stably stratified overlaying layer.

449 The transient behavior after this time is very similar to  $M_g = 0$  up to ( $M_g = 0.4$ ,  $\Delta\theta = -10$ ),  
450 but the LSBs are more accelerated because of the directionality of the advected inflows  
451 along  $\alpha = 0^\circ$ . Further decrease of the thermal contrast in the subplot ( $M_g = 0.4$ ,  $\Delta\theta_2 = -5$ )  
452 results in a transitional regime where the canonical LB loses its shape as result of the  
453 advected inflows that are trying to keep the sea neutral. Therefore, any canonical LB is  
454 short-lived along this direction. Also, canonical SBs require more heating over land  
455 because the sea tends to establish neutral stratification (because of inflows), and therefore  
456 the heat flux contrast across the whole ABL depth between land and sea is diminished  
457 compared to the  $M_g = 0$  transient behavior.

458 The transient dynamics for larger pressure forcings (subplots of  $M_g = 1.2$  and 2) result in  
459 almost advected LSBs (exceptions for  $\Delta\theta_2 = 5$ ,  $\Delta\theta_2 = 0$ ,  $\Delta\theta_1 = -5$  at  $M_g = 1.2$ ). LSBs weakly  
460 resist the pronounced increase of the pressure forcing here as the air over the sea remains  
461 neutral, and the flow over land goes from mildly to extremely unstable. However, these  
462 LSBs are boosted by buoyancy as their strength exceeds sometimes  $M_g$ . One remark here  
463 (for both  $M_g = 1.2$  and 2) is that the canonical LB does not form any more; instead, an  
464 extremely persistent shallow micro-LB forms near the surface at night. This micro-LB is  
465 similar to a density current that could trigger turbulence intermittency at the finest scales  
466 over land and nearby sea (see Mahrt (2010) Allouche et al. (2022) for other intermittency  
467 triggering mechanisms). The LB's leading edge protrudes the furthest into the sea for the  
468 maximum buoyant destruction attained at  $\Delta\theta_2 = -5$ , as it resists the strengthened incoming  
469 inflows.

470 The top panel in Fig. 7 (like Fig. 5), shows  $R(t)$  and the averaged enstrophy  $\mathcal{E}(t)$  for  $\alpha = 0^\circ$   
471 (here the correlation is relative to the steady cases with the same  $M_g$  and  $\alpha$ ).  $R(t)$  increases  
472 gradually following the time corresponding to  $\theta_L = \theta_{max}$  and eventually reaches  $R_{max} = 0.15$   
473 for  $M_g = 0.4$ ,  $R_{max} = 0.81$  for  $M_g = 1.2$ , and  $R_{max} = 0.85$  for  $M_g = 2$ . As expected,  $R(t)$  attains  
474 higher maximum values as  $M_g$  increases (transient thermal dynamics become less  
475 important). Moreover, at weaker  $M_g$ , the likelihood of recovering the corresponding  
476 steady state LSB is limited since memory effects play a critical role in modulating the

477 resultant dynamics. All cases, however, have a comparable time lag to peak correlation of  
 478 about  $\tau_{lag}=7$ -hour relative to the SS circulation to  $\theta_L=\theta_{max}$ . Almost, the same  $\tau_{lag}$  reported  
 479 for  $M_g=0$  (subsection 5.1) qualifies here as well for  $\alpha=0^\circ$  at all  $M_g$ . We also note here that  
 480 the averaged enstrophy  $\varepsilon(t)$  trends (for all  $M_g$ ) peak almost at the time corresponding to  
 481 such a characteristic lag ( $\tau_{lag}$ ). Beyond this lag, both  $R(t)$  and  $\varepsilon(t)$  drop significantly.

### 482 5.3 Transient LSBs along $\alpha=180^\circ$

483 Here, a land-to-sea pressure gradient is imposed, along with Y-Z inflow slices of the  
 484 dynamics and thermal structures of diurnal flow over an infinite land. The subplot  $\{M_g$   
 485  $=0.4, \Delta\theta_1=0\}$  in Fig. 4 demonstrates a transitional regime where residuals of the night  
 486 land breeze are still observed (the LB here is much stronger than the LB corresponding to  
 487  $\alpha=0^\circ$  as it is aided by the inflows). One important remark is that the leading edge of this  
 488 land breeze prevails further downstream over the sea compared to  $\alpha=0^\circ$ .

489 As the land heats up, accompanied by the advection of strengthened unstable structures in  
 490 the subplot ( $M_g=0.4, \Delta\theta_1=5$ ), mixing is increased over land and the unstable boundary  
 491 layer near the surface deepens more rapidly. These simultaneous mechanisms facilitate  
 492 the eradication of the mildly stably stratified overlaying layer. With further increase in  
 493 the thermal contrast in the subplot ( $M_g=0.4, \Delta\theta=10$ ), SB initiation starts here earlier  
 494 compared to  $\alpha=0^\circ$ , but the advection of thermal convective rolls from land to sea hinders  
 495 the SB front inland penetration where it stalls near the shore at  $X=43$  km. The SB hardly  
 496 penetrates in the subplot ( $M_g=0.4, \Delta\theta_2=5$ ), as it is resisted by the advected structures. In  
 497 the subsequent subplot ( $M_g=0.4, \Delta\theta_2=0$ ), the SB continues to strengthen as buoyancy  
 498 here is still being boosted inland ( $\Delta\theta \geq 0$ ) and diminished over the sea patch because the  
 499 advected inflows render the sea more stable with respect to time, and therefore this makes  
 500 the SB more persistent. In the subplot ( $M_g=0.4, \Delta\theta_1=-5$ ), the LSB continues to transition  
 501 as the potential LB formation is dynamically and thermally aided near the surface by the  
 502 stably advected inflows. In the subplot ( $M_g=0.4, \Delta\theta=-10$ ), a canonical LB forms, which  
 503 then begins to fade in the subsequent subplot ( $M_g=0.4, \Delta\theta_2=-5$ ) as stability over land is  
 504 weakened. The advected inflows at this stage easily destroy this canonical LB and  
 505 replaces it with a transition regime LSB in subplot ( $M_g=0.4, \Delta\theta_1=0$ ).

506 The transient dynamics for larger pressure forcings (subplots of  $M_g = 1.2$  and 2) result  
 507 only in land-driven SBs for  $\Delta\theta=10$ ,  $\Delta\theta_2=5$ , and  $\Delta\theta_2=0$  for both  $M_g$ 's and advected LSBs  
 508 for all other  $\Delta\theta$ 's (canonical LSBs do not form anymore). In a nutshell (along  $\alpha=180^\circ$ ), as  
 509 the land heats during the day, amplified advection of unstable inflows ensues and renders  
 510 the land more unstable and the sea more stable. Therefore, SB initiation is favored to start  
 511 earlier (compared to  $\alpha=0^\circ$ ), and as the pressure forcing increases, it persists longer (as  
 512 this correlates with stronger stabilities over the sea) but its front is strongly impeded  
 513 inland (because of the strengthened opposing inflows). During nighttime, as the land  
 514 starts cooling, aided by the stably advected inflows, the sea inherits a stably stratified  
 515 thermal memory that inhibits its regime shift until much later into the night, and thus  
 516 remains almost neutral at that stage. Therefore, LB formation is not favored (especially in  
 517 its canonical shape).

518 The bottom panel in Fig. 7, shows  $R(t)$  and the averaged enstrophy  $\mathcal{E}(t)$  for  $\alpha=180^\circ$ . For  
 519  $M_g = 0.4$ ,  $R(t)$  increases following the time corresponding to  $\theta_L=\theta_{max}$  and reaches  
 520  $R_{max}=0.78 \gg R_{max}=0.15$  for  $\alpha=0^\circ$ . For  $M_g = 1.2$  and 2 respectively,  $R(t)$  almost plateaus  
 521 during this time and reaches  $R_{max}=0.41 \ll R_{max}=0.81$  for  $\alpha=0^\circ$ , and  $R_{max}=0.68 <$   
 522  $R_{max}=0.85$  for  $\alpha=0^\circ$ .  $R_{max}$  values here change in a non-monotonic sense as  $M_g$  increases.  
 523 An approximate characteristic lag of  $\tau_{lag}=5$ -hour relative to the SS time corresponding to  
 524  $\theta_L=\theta_{max}$  is found here. The fact that  $(\tau_{lag}=5\text{-hour here for } \alpha=180^\circ) < (\tau_{lag}=7\text{-hour for } \alpha=0^\circ$   
 525 and for  $M_g=0)$  can be attributed to the nature of these transient inflows, which causes  
 526 land-driven SBs to initiate earlier as described in the transient dynamics above, and thus  
 527 faster recovery of the corresponding SS LSB if achieved. Remarkably here for  $\alpha=180^\circ$   
 528 and unlike  $\alpha=0^\circ$ , beyond the identified lag (that is for  $t > \tau_{lag}=5\text{-hour}$ ), the drop in  $R(t)$  is  
 529 accompanied by a sharp increase in the averaged enstrophy  $\mathcal{E}(t)$  for all  $M_g$ .

## 530 **6 Surface and shore exchanges**

### 531 *6.1 Surface exchanges*

532 We plot in Fig. 8 the diurnal profiles of the surface heat flux  $(\overline{w'\theta'})$  for both directions  
 533 ( $\alpha=0^\circ$  and  $\alpha=180^\circ$ ) over the two analysis patches, sea and land. For  $M_g=0$ , and as  
 534 described in the previous subsection 5.1,  $\overline{w'\theta'}_{sea}$  is positive (unstable) at  $t=0$  before the

land starts heating up because of the prevailing cool nighttime land breeze. As we progress in time,  $\overline{w'\theta'}_{sea}$  drops to almost zero at  $t=6$  h ( $\Delta\theta=\Delta\theta_{max}$ ), i.e., a neutral sea. Note that the sea remains neutral at such thermal contrast and for most of the daytime, while in the steady state cases it is slightly stable. This is attributed to the memory effects of the persistent thermal boundary layer associated with the previously established near-surface land breeze. At  $t=18$  h ( $\Delta\theta=-\Delta\theta_{max}$ ), a canonical land breeze develops, and the sea returns gradually to an unstable condition at the end of the cycle at  $t=24$  h ( $\Delta\theta=0$ ). Therefore,  $\overline{w'\theta'}_{sea}$  reveals a strong hysteresis for the  $M_g=0$ .

Along  $\alpha=0^\circ$  and as  $M_g$  increases ( $M_g=0.4$  ms<sup>-1</sup> subplot), this hysteretic response is weakened especially when  $\Delta\theta>0$ , and the observed  $\overline{w'\theta'}_{sea}$  unstable maximum value reduces by almost one order of magnitude (relative to  $M_g=0$  ms<sup>-1</sup>) because of the neutral sea advected inflows. For  $M_g=2$ , the hysteresis is eliminated when  $\Delta\theta>0$ , but persists marginally when  $\Delta\theta<0$  because of the land breeze transient penetration over the sea. An important note here is that, if we average the sea surface heat flux by excluding dynamically (with respect to time) the sea sub patch where this land breeze prevails, the hysteresis response would be fully eliminated when ( $\Delta\theta<0$ , not shown here). This implies that the hysteresis is directly linked to the breeze dynamics near the shore. The friction velocity,  $\bar{u}_{*sea}$ , experiences similar trends, but displays weaker hysteresis compared to  $\overline{w'\theta'}_{sea}$ , and such type of response is completely eliminated for  $M_g=2$  (not shown here).

In the same Fig. 8, over land with  $M_g=0$ ,  $\overline{w'\theta'}_{Land}$  is positive (unstable) when  $\Delta\theta>0$  and negative (stable) almost for every point when  $\Delta\theta<0$ . The range of variability here for  $\overline{w'\theta'}_{Land}$  is almost four times greater than  $\overline{w'\theta'}_{sea}$ , and a much weaker hysteresis is observed over land. The relatively higher fluxes over land imply that land is the primarily driver of these LSBs, whereas the sea is adaptively responding to the former's transient dynamics. Note that the reported  $\overline{w'\theta'}_{Land} \approx 0.06$  K m/s at  $t=6$  h ( $\Delta\theta=\Delta\theta_{max}$ ) is almost the same as the steady state value we observed in ABI23. As  $M_g$  increases along  $\alpha=0^\circ$  ( $M_g=0.4$  subplot), the hysteresis is mildly strengthened especially when ( $\Delta\theta>0$ ) because both buoyancy and shear are co-modulating the transient LSBs. For  $M_g=2$ , such type of response is almost fully eliminated. For  $\alpha=0^\circ$  and  $M_g>0$ , the reported heat fluxes  $\overline{w'\theta'}_{Land} \approx 0.06$  K m/s at  $t=6$  h ( $\Delta\theta=\Delta\theta_{max}$ ) are almost half the steady state reported

565 values because  $\Delta\theta$  is not maintained at its maximum  $\Delta\theta_{max}$ . The friction velocity,  $\bar{u}_{*Land}$   
 566 reveals stronger hysteresis response compared to  $\overline{w'\theta'}_{Land}$ , and these responses are never  
 567 eliminated even for  $M_g=2$  (not shown here).

568 Now along  $\alpha=180^\circ$ , as  $M_g$  increases ( $M_g=0.4$  subplot),  $\overline{w'\theta'}_{sea}$  shows a strengthened  
 569 hysteretic response compared to  $\alpha=0^\circ$ , and  $\overline{w'\theta'}_{sea} \approx -1.5 \times 10^{-3}$  K m/s reaches a new  
 570 minimum attributed to the diurnal land inflows, which augments the negative heat flux  
 571 over the sea (stable, refer to the physical analysis in subsection 5.3). For  $M_g=2$ , such  
 572 response is strengthened further because of the intensified diurnal land inflow planes  
 573 where  $\overline{w'\theta'}_{sea} \approx -5 \times 10^{-3}$  more than triples relative to  $M_g=0.4$ . For  $M_g=0.4$  and  $M_g=2$ ,  
 574 the reported heat fluxes  $\overline{w'\theta'}_{sea} \approx -0.3 \times 10^{-3}$  K m/s and  $\overline{w'\theta'}_{sea} \approx -1.4 \times 10^{-3}$  K  
 575 m/s at  $t=6$  h ( $\Delta\theta=\Delta\theta_{max}$ ) are around 5% and 12% the steady state values in ABI23, again  
 576 because  $\Delta\theta$  is not maintained at its maximum  $\Delta\theta_{max}$ . In addition, the friction velocity,  
 577  $\bar{u}_{*sea}$  experience a similar but weaker hysteresis (not shown here). Over the land patch  
 578 and as  $M_g$  increases here along  $\alpha=180^\circ$  ( $M_g=0.4$  subplot),  $\overline{w'\theta'}_{Land}$  shows a weakened  
 579 hysteresis response compared to  $\alpha=0^\circ$  because of the diurnal land inflows along this  
 580 direction especially when  $\Delta\theta>0$ . For  $M_g=2$ , the hysteresis response is almost fully  
 581 eliminated as with the corresponding  $\alpha=0^\circ$  case. For  $\alpha=180^\circ$  and  $M_g>0$ , the reported heat  
 582 fluxes  $\overline{w'\theta'}_{Land} \approx 0.04$  K m/s at  $t=6$  h ( $\Delta\theta=\Delta\theta_{max}$ ) are almost one third the steady state  
 583 values. Also, the friction velocity,  $\bar{u}_{*Land}$  shows stronger hysteresis responses compared  
 584 to  $\overline{w'\theta'}_{Land}$  (not shown here).

585 In a nutshell, the land surface heat flux hysteresis response is weakened as  $M_g$  increases,  
 586 and is almost eliminated for  $M_g=2$ . However, the sea surface heat flux hysteresis is  
 587 strengthened for  $M_g=2$  ( $\alpha=180^\circ$ ), and significantly weakened but never eliminated for  
 588  $\alpha=0^\circ$  because of the prevailing near surface land breeze here. Hence, a sea surface heat  
 589 flux hysteresis is always exhibited anytime the diurnal LSBs are passing through any of  
 590 the canonical reference states LSB types (canonical SB, canonical LB, land-driven SB).  
 591 Note that purely diurnal advected LSBs might still show a very weak  $\overline{w'\theta'}_{sea}$  hysteretic  
 592 response when micro LBs or SBs prevail. This is discerned for  $M_g=2$  along  $\alpha=0^\circ$  when  
 593 the shallow near surface LBs persist, or as could be anticipated for  $M_g>2$  along  $\alpha=180^\circ$   
 594 since the shallow land-driven SBs would still form (not simulated here).

595 **6.2 Mean flow and turbulence at the shore**

596  $Q_{shore}$  is defined here as the net volumetric flux across a unit along-shore width,  $\|y_n\|=1$  m  
 597 (added merely for convenience in interpreting units), at the shore interface  $X=40$  km.  $Q_{sc}$   
 598 represents a normalized version of  $Q_{shore}$ , and both are defined below:

$$Q_{shore} = \frac{\|y_n\|}{L_y} \int_0^{L_y} \int_{z_0}^{L_z} U_{shore} dz dy, \quad (4)$$

$$Q_{sc} = \frac{Q_{shore}}{M_g L_z \|y_n\|} = \frac{1}{L_z L_y M_g} \int_0^{L_y} \int_{z_0}^{L_z} U_{shore} dz dy. \quad (5)$$

599 Fig. 9 shows the diurnal variation  $Q_{sc}$  for each  $\alpha$  with increasing  $M_g$ , with respect to the  
 600 surface forcing  $\Delta\theta(t)$  and turbulent kinetic energy at the shore ( $e_{shore}$ , averaged in the  
 601 same way as  $Q_{shore}$ ). We do not plot the case with  $M_g = 0$  since the shore flux in these is  
 602 nearly zero. Along  $\alpha=0^\circ$  and as  $M_g$  increases, the  $\{Q_{sc}, \Delta\theta(t)\}$  and  $\{Q_{sc}, e_{shore}\}$  hysteretic  
 603 responses are weakened and then almost eliminated for  $M_g=2$ . One can even observe one  
 604 case of quasi-equilibrium for  $\alpha=0^\circ$  and  $M_g=2$ . However, along  $\alpha=180^\circ$  and as  $M_g$   
 605 increases, the  $\{Q_{sc}, \Delta\theta(t)\}$  and  $\{Q_{sc}, e_{shore}\}$  responses are strengthened and more  
 606 hysteretic, and we do not discern any case of quasi-equilibrium for the simulated cases.

607 For both directions, the mean flow is out of equilibrium with turbulence anytime the sea  
 608 surface heat flux shows a significant hysteretic behavior as depicted in Fig. 8. The fact  
 609 that the land patch exhibits stronger surface heat fluxes than the sea and much weaker  
 610 hysteretic responses as  $M_g$  increases does not guarantee attaining turbulence equilibrium  
 611 with the mean; therefore, the final turbulence-mean flow equilibrium response is quite  
 612 sensitive to the sea surface heat flux behavior as well.

613 Note that the reported  $Q_{sc}$  values along  $\alpha=0^\circ$  at  $t=6$  h ( $\Delta\theta=\Delta\theta_{max}$ )  $\{Q_{sc}=1.29$  for  $M_g=0.4$ ,  
 614  $Q_{sc}=1.08$  for  $M_g=1.2$ ,  $Q_{sc}=1.05$  for  $M_g=2\}$  are almost the same as their corresponding  
 615 steady state reported values. Along  $\alpha=180^\circ$ , the reported  $Q_{sc}$  values at  $t=6$  h ( $\Delta\theta=\Delta\theta_{max}$ )  
 616  $\{Q_{sc}=-0.72$  for  $M_g=0.4$ ,  $Q_{sc}=-0.86$  for  $M_g=1.2$ ,  $Q_{sc}=-0.91$  for  $M_g=2\}$  are slightly  
 617 different than their corresponding steady state values  $\{Q_{sc}=-0.69$  for  $M_g=0.4$ ,  $Q_{sc}=-0.91$   
 618 for  $M_g=1.2$ ,  $Q_{sc}=-0.95$  for  $M_g=2\}$  because of the inherent memory effects and the nature

of the continuously evolving inflows fed in the main unsteady simulation. For  $M_g > 0.4$ , both the steady state and unsteady simulations result in land driven LSBs at  $t=6$  h, but more mass flux occurs in the steady state simulations because of the fact that  $\Delta\theta$  is maintained at its maximum  $\Delta\theta_{max}$ , which results in shallower land-driven LSBs.

## 7 Macro and micro LSBs categorization

Visual inspection and previous analysis of the thermal circulations large scale flow structures in sections 4 and 5 reveal four types of LSBs: (i) canonical LSBs of two flavors, Canonical-CCW SB (CCW: counter-clockwise LSB) and Canonical-CW LB (CW: clockwise LSB); (ii) a Transitional LSB, (iii) a Land-driven SB, and (iv) advected LSBs of two flavors, Advected-SL LSBs (SL: sea to land) or Advected-LS LSBs (LS: land to sea). Therefore, we consider the vertical profile of the shore-normal velocity  $\bar{U}(z)$  at the shoreline,  $\bar{U}(z)_{shore}$ , with the aid of the  $k$ -means clustering algorithm (Lloyd, 1982), to delineate these circulations without any human visual inspection. This autonomous algorithm is provided with  $\bar{U}(z)_{shore}$  as an input (only for the last two cycle to have more training data), and the number of the desired clusters (= 6 as depicted) is specified as well. The top panel of Fig. 10 shows the macro-classification results that are overlaid on the land surface temperature profile to easily track the evolution of the identified regimes. As could be inferred from the movies and section 5, the clustered data here (as learnt from the vertical profiles of  $\bar{U}(z)_{shore}$ ) reflect their corresponding regimes most of the time, except when the LSB is about to shift regime and the classification is more uncertain.

The top panel of Fig. 10 depicts the large-scale evolution of the clustered LSBs in the entire ABL, but that does not necessarily reflect what is happening very near the surface. Therefore, in the bottom panel of Fig. 10, we consider the streamwise profile of the shore-normal velocity  $\bar{U}(x) - z_1$  at the first grid level above the surface ( $z_1$ ), also with the aid of  $k$ -means clustering algorithm to produce a micro-classification of the regimes. The number of the desired clusters is here set to 4 here because this corresponds to the observed air dynamics over the two patches as will be explained shortly. The exponent sign symbol here represents the air direction over each patch, and the number of signs denotes the relative strength in air dynamics: (i)  $S^+L^+$ : air is fully advected from sea to

land through all  $L_x$ , (ii)  $S^+L^-$ : air over land tends to penetrate the sea patch, i.e., the prevailing nighttime shallow land breeze for the case of  $\alpha=0^\circ$ ,  $M_g>0.4$  (clearly seen in the movies), (iii)  $S^{++}L^-$ : air over sea tends to penetrate the land patch, i.e., the land-driven SB for the case of  $\alpha=180^\circ$ , mainly at  $M_g>0.4$  (clearly seen in the movies), (iv)  $S^-L^-$ : air is fully advected from land to sea through all  $L_x$ . The near surface air dynamics are fairly captured with such a  $\bar{U}(x) - z_1$  micro-classification. One can note a correspondence of the bulk classification in the top panel of Fig. 10 with the surface micro classification in the bottom panel, but the timing of the transition and some details are not identical. This implies that surface measurements do not fully characterize the LSB regime.

## 8 Conclusion and implications

LES modeling of the unsteady LSBs, in the presence of constant synoptic pressure forcing along the symmetric directions  $\alpha=0^\circ$  and  $\alpha=180^\circ$ , reveals four different regimes: (i) canonical LSB, (ii) transitional LSB, (iii) land-driven SB, (iv) advected LSB. The first two types (i) and (ii) emerge when the synoptic forcing is weak ( $M_g=0$  and  $0.4$ ) for both directions, and the LSB is shown to be transitional anytime it is shifting between the two canonical reference states “SB and LB”. When the synoptic forcing strengthens along  $\alpha=0^\circ$ , both canonical SB and advected LSB regimes are present at different times for  $M_g=1.2$ , while only purely advected LSBs are found for  $M_g=2$ . However, along  $\alpha=180^\circ$ , land-driven SB and advected LSB regimes persist even up to the highest simulated case  $M_g=2$ . In addition to the different interactions with the breeze circulations of the synoptic wind blowing from either direction, an important contributor to the difference for these transient cases is the asymmetry of the inherent inflows: for  $\alpha=0^\circ$  they consist of streamwise rolls with neutral stability, while and  $\alpha=180^\circ$ , they feature stably stratified turbulence during nighttime and thermal convection during the unstable daytime. In addition, these inflows interact with an evolving diurnal thermal circulation that is modulated by its thermal and kinetic inertias, found to be influential under weak synoptic forcings ( $M_g=0$  and  $0.4$ ) for both directions ( $\alpha=0^\circ$  and  $\alpha=180^\circ$ ).

Focusing on the transient dynamics of the cases with stronger pressure forcings ( $M_g=1.2$  and  $2$ ), along  $\alpha=180^\circ$ , land-driven SBs initiation can start earlier in time (compared to  $\alpha=0^\circ$ ) because of the advected unstable inflows, but they fade away earlier too. In



679 addition, land-driven SBs persists longer as  $M_g$  increases along  $\alpha=180^\circ$  (because the  
 680 strengthened land advected unstable inflows correlate with stronger negative heat fluxes  
 681 over sea), whereas canonical SBs shift to an advected LSB reference type along  $\alpha=0^\circ$   
 682 (because the strengthened sea advected neutral inflows correlate with stronger positive  
 683 heat fluxes over land). As the land starts cooling, along  $\alpha=180^\circ$ , the sea still inherits a  
 684 stable thermal memory that strengthens with time (because of the stably advected  
 685 inflows), instead of weakening, and inhibits canonical LB formation. During the same  
 686 time but along  $\alpha=0^\circ$ , a micro (near surface) land breeze forms and prevails throughout the  
 687 negative thermal contrast and beyond.

688 These dynamics often result in non-equilibrium flows over the two patches that manifest  
 689 as a hysteresis in the response of the turbulence to the mean flow, as well as the response  
 690 of the mean flow to the driving temperature contrast. This confirm that the mean flow has  
 691 a significant memory that induces this hysteresis relative to the external forcing, and that  
 692 the mean flow variability is too rapid for turbulence to equilibrate. Hysteresis is thus  
 693 noted when the turbulent land surface fluxes over the diurnal cycle are plotted versus the  
 694 temperature contrast, but this hysteresis is noticeably undermined when  $M_g$  increases for  
 695 both directions. On the other hand, the sea surface heat flux hysteresis relative to the  
 696 temperature contrast is strengthened for  $M_g=2$  at  $\alpha=180^\circ$ , but substantially weakened yet  
 697 never eliminated for  $\alpha=0^\circ$  because of the persistent micro land breeze. The sea surface  
 698 heat flux hysteresis persists anytime the diurnal LSBs pass through any of the canonical  
 699 reference state LSB types (canonical SB, canonical LB, and land-driven SB). Advected  
 700 LSBs are found to eliminate  $\overline{w'\theta'}_{sea}$  hysteresis, but any potential formation of either  
 701 micro-SB or micro-LB during the day perturbs the response and pushes it back to a mild  
 702 hysteretic type.

703 Similarly, the diurnal variation of the normalized net shore volumetric flux shows a  
 704 hysteretic response for  $\alpha=180^\circ$  as  $M_g$  increases, but not for  $\alpha=0^\circ$ . It is noticed that as  $M_g$   
 705 increases (especially for  $\alpha=0^\circ$ ), i.e., the flow tends to be pressure gradient dominated, the  
 706 hysteretic response of either surface heat fluxes ( $\overline{w'\theta'}$ ,  $\Delta\theta(t)$ ), or shoreline mean-flow  
 707 ( $Q_{sc}$ ,  $\Delta\theta(t)$ ) and ( $Q_{sc}$ ,  $e_{shore}$ ) is undermined or almost eliminated. In fact, we observe only  
 708 one case of equilibrium that corresponds to ( $\alpha=0^\circ$  and  $M_g=2$ ) in the simulated cases. The

mean flow is found to be out of equilibrium with turbulence anytime the sea surface heat flux response shows a substantial hysteretic response with the external forcing despite the fact that the land patch converges to equilibrium faster as  $M_g$  increases. For the simulated cases along  $\alpha=180^\circ$ , we observe a strengthened hysteric response  $(\overline{w'\theta'}_{sea}, \Delta\theta(t))$  as  $M_g$  increases because of the persistent land-driven SB, which in turn pushes the shoreline mean-flow response either  $(Q_{sc}, \Delta\theta(t))$  or  $(Q_{sc}, e_{shore})$  into non-equilibrium.

Finally, the vertical profile of the shore-normal velocity  $\bar{U}(z)$  can be used with  $k$ -means clustering to delineate the large-scale evolution of the clustered LSBs in the entire ABL (macro categorization). Similarly, the stream-wise profile of the shore-normal velocity  $\bar{U}(x) - z_1$  at the first grid level above the surface is used to demarcate the near-surface evolution of the LSBs (micro categorization). Both methods are tested, and they are found to complement each other in offering a descriptive picture of the resultant transient LSBs especially when micro-SBs or micro-LBs form with an advected LSB background regime.

This analysis offers insights into the dynamics and non-equilibrium of these LSBs on either side of the shore. The impacts on airflow, surface fluxes, cross-shore transport and multiple flow characteristics are significant and cannot be ignored in models that do not resolve this coastal sub-grid scale surface heterogeneity adequately. The potential implications of such a behavior are non-local because of the compounded and nonlinear interactions between rainfall, temperature, radiative effects, wind, humidity, and cloud formation during the time it takes the transient surface information to be communicated to the atmosphere. Incorporating these dynamics in such models (coarse weather and climate models) is thus an essential task, but as this study shows a challenging one due to the many embedded time-varying inputs, implicit memory effects and unresolved processes.

## Acknowledgments

M.A. and E.B.Z. are supported by the Cooperative Institute for Modeling the Earth System at Princeton University under Award NA18OAR4320123 from the National Oceanic and Atmospheric Administration, and by the US National Science Foundation

under award number AGS 2128345. The LES are conducted on the Cheyenne supercomputer of the National Center for Atmospheric Research (doi:10.5065/D6RX99HX) under projects UPRI0007 and UPRI0021. The authors declare no conflict of interest.

## Data availability

The dataset of all the LES simulations are publicly available at <https://doi.org/10.5281/zenodo.10433810> (Allouche et al. [2023]).

## References

- Ado, H. Y. (1992). Numerical Study of the Daytime Urban Effect and Its Interaction with the Sea Breeze. *Journal of Applied Meteorology*, 31(10), 1146–1164.  
[https://doi.org/10.1175/1520-0450\(1992\)031<1146:NSOTDU>2.0.CO;2](https://doi.org/10.1175/1520-0450(1992)031<1146:NSOTDU>2.0.CO;2)
- Allouche, M., Bou-Zeid, E., Ansorge, C., Katul, G. G., Chamecki, M., Acevedo, O., Thanekar, S., & Fuentes, J. D. (2022). The Detection, Genesis, and Modeling of Turbulence Intermittency in the Stable Atmospheric Surface Layer. *Journal of the Atmospheric Sciences*, 79(4), 1171–1190. <https://doi.org/10.1175/JAS-D-21-0053.1>
- Allouche, M., Bou-Zeid, E., & Lipponen, J. (2023). The influence of synoptic wind on land–sea breezes. *Quarterly Journal of the Royal Meteorological Society*, 149(757), 3198–3219. <https://doi.org/10.1002/qj.4552>
- Antonelli, M., & Rotunno, R. (2007). Large-eddy simulation of the onset of the sea breeze. *Journal of the Atmospheric Sciences*.  
<https://doi.org/10.1175/2007JAS2261.1>
- Atkison, B. W. (1995). Sea breeze and local wind. By J. E. Simpson. Cambridge University Press. 1994. Pp. 234. Price £29.95 (hardback). ISBN 0 521 452112. *Quarterly Journal of the Royal Meteorological Society*.  
<https://doi.org/10.1002/qj.49712152315>
- Bauer, T. J. (2020). Interaction of Urban Heat Island Effects and Land–Sea Breezes during a New York City Heat Event. *Journal of Applied Meteorology and Climatology*, 59(3), 477–495. <https://doi.org/10.1175/JAMC-D-19-0061.1>
- Bou-Zeid, E., Anderson, W., Katul, G. G., & Mahrt, L. (2020a). The Persistent Challenge of Surface Heterogeneity in Boundary-Layer Meteorology: A Review. *Boundary-*

- 768 *Layer Meteorology*, 177(2–3), 227–245. [https://doi.org/10.1007/s10546-020-00551-](https://doi.org/10.1007/s10546-020-00551-8)  
769 8
- 770 Bou-Zeid, E., Anderson, W., Katul, G. G., & Mahrt, L. (2020b). The Persistent Challenge  
771 of Surface Heterogeneity in Boundary-Layer Meteorology: A Review. *Boundary-*  
772 *Layer Meteorology*. <https://doi.org/10.1007/s10546-020-00551-8>
- 773 Bou-Zeid, E., Meneveau, C., & Parlange, M. (2005). A scale-dependent Lagrangian  
774 dynamic model for large eddy simulation of complex turbulent flows. *Physics of*  
775 *Fluids*. <https://doi.org/10.1063/1.1839152>
- 776 Cana, L., Grisolia-Santos, D., & Hernández-Guerra, A. (2020). A Numerical Study of a  
777 Sea Breeze at Fuerteventura Island, Canary Islands, Spain. *Boundary-Layer*  
778 *Meteorology*. <https://doi.org/10.1007/s10546-020-00506-z>
- 779 Cioni, G., & Hohenegger, C. (2018). A simplified model of precipitation enhancement  
780 over a heterogeneous surface. *Hydrology and Earth System Sciences*.  
781 <https://doi.org/10.5194/hess-22-3197-2018>
- 782 Dailey, P. S., & Fovell, R. G. (1999). Numerical Simulation of the Interaction between  
783 the Sea-Breeze Front and Horizontal Convective Rolls. Part I: Offshore Ambient  
784 Flow. *Monthly Weather Review*, 127(5), 858–878. [https://doi.org/10.1175/1520-](https://doi.org/10.1175/1520-0493(1999)127<0858:NSOTIB>2.0.CO;2)  
785 0493(1999)127<0858:NSOTIB>2.0.CO;2
- 786 Díaz, H., & Guedes Soares, C. (2020). Review of the current status, technology and  
787 future trends of offshore wind farms. *Ocean Engineering*, 209, 107381.  
788 <https://doi.org/10.1016/j.oceaneng.2020.107381>
- 789 Fovell, R. G., & Dailey, P. S. (2001). Numerical Simulation of the Interaction between  
790 the Sea-Breeze Front and Horizontal Convective Rolls. Part II: Alongshore Ambient  
791 Flow. *Monthly Weather Review*, 129(8), 2057–2072. [https://doi.org/10.1175/1520-](https://doi.org/10.1175/1520-0493(2001)129<2057:NSOTIB>2.0.CO;2)  
792 0493(2001)129<2057:NSOTIB>2.0.CO;2
- 793 Fu, S., Rotunno, R., Chen, J., Deng, X., & Xue, H. (2021). A large-eddy simulation study  
794 of deep-convection initiation through the collision of two sea-breeze fronts.  
795 *Atmospheric Chemistry and Physics*, 21(12), 9289–9308.  
796 <https://doi.org/10.5194/acp-21-9289-2021>

- 797 Ghannam, K., & Bou-Zeid, E. (2021). Baroclinicity and directional shear explain  
798 departures from the logarithmic wind profile. *Quarterly Journal of the Royal  
799 Meteorological Society*. <https://doi.org/10.1002/qj.3927>
- 800 Howland, M. F., González, C. M., Martínez, J. J. P., Quesada, J. B., Larrañaga, F. P.,  
801 Yadav, N. K., Chawla, J. S., & Dabiri, J. O. (2020). Influence of atmospheric  
802 conditions on the power production of utility-scale wind turbines in yaw  
803 misalignment. *Journal of Renewable and Sustainable Energy*.  
804 <https://doi.org/10.1063/5.0023746>
- 805 Huang, J., & Bou-Zeid, E. (2013). Turbulence and Vertical Fluxes in the Stable  
806 Atmospheric Boundary Layer. Part I: A Large-Eddy Simulation Study. *Journal of  
807 the Atmospheric Sciences*. <https://doi.org/10.1175/jas-d-12-0167.1>
- 808 Huang, J., Bou-Zeid, E., & Golaz, J.-C. (2013). Turbulence and Vertical Fluxes in the  
809 Stable Atmospheric Boundary Layer. Part II: A Novel Mixing-Length Model.  
810 *Journal of the Atmospheric Sciences*. <https://doi.org/10.1175/JAS-D-12-0168.1>
- 811 Jiang, P., Wen, Z., Sha, W., & Chen, G. (2017). Interaction between turbulent flow and  
812 sea breeze front over urban-like coast in large-eddy simulation. *Journal of  
813 Geophysical Research: Atmospheres*, 122(10), 5298–5315.  
814 <https://doi.org/10.1002/2016JD026247>
- 815 Kumar, V., Kleissl, J., Meneveau, C., & Parlange, M. B. (2006). Large-eddy simulation  
816 of a diurnal cycle of the atmospheric boundary layer: Atmospheric stability and  
817 scaling issues. *Water Resources Research*. <https://doi.org/10.1029/2005WR004651>
- 818 Kumer, V. M., Reuder, J., Dörninger, M., Zauner, R., & Grubišić, V. (2016). Turbulent  
819 kinetic energy estimates from profiling wind LiDAR measurements and their  
820 potential for wind energy applications. *Renewable Energy*.  
821 <https://doi.org/10.1016/j.renene.2016.07.014>
- 822 Lembo, V., Lunkeit, F., & Lucarini, V. (2019). TheDiaTo (v1.0) – a new diagnostic tool  
823 for water, energy and entropy budgets in climate models. *Geoscientific Model  
824 Development*, 12(8), 3805–3834. <https://doi.org/10.5194/gmd-12-3805-2019>
- 825 Levy, I., Mahrer, Y., & Dayan, U. (2009). Coastal and synoptic recirculation affecting air  
826 pollutants dispersion: A numerical study. *Atmospheric Environment*, 43(12), 1991–  
827 1999. <https://doi.org/10.1016/j.atmosenv.2009.01.017>

- 828 Lin, C.-Y., Chen, F., Huang, J. C., Chen, W.-C., Liou, Y.-A., Chen, W.-N., & Liu, S.-C.  
829 (2008). Urban heat island effect and its impact on boundary layer development and  
830 land–sea circulation over northern Taiwan. *Atmospheric Environment*, 42(22),  
831 5635–5649. <https://doi.org/10.1016/j.atmosenv.2008.03.015>
- 832 Llaguno-Munitxa, M., & Bou-Zeid, E. (2018). Shaping buildings to promote street  
833 ventilation: A large-eddy simulation study. *Urban Climate*.  
834 <https://doi.org/10.1016/j.uclim.2018.08.006>
- 835 Lo, J. C. F., Lau, A. K. H., Fung, J. C. H., & Chen, F. (2006). Investigation of enhanced  
836 cross-city transport and trapping of air pollutants by coastal and urban land-sea  
837 breeze circulations. *Journal of Geophysical Research*, 111(D14), D14104.  
838 <https://doi.org/10.1029/2005JD006837>
- 839 Lund, T. S., Wu, X., & Squires, K. D. (1998). Generation of Turbulent Inflow Data for  
840 Spatially-Developing Boundary Layer Simulations. *Journal of Computational*  
841 *Physics*. <https://doi.org/10.1006/jcph.1998.5882>
- 842 Lyons, W. (1995). Modeling impacts of mesoscale vertical motions upon coastal zone air  
843 pollution dispersion. *Atmospheric Environment*, 29(2), 283–301.  
844 [https://doi.org/10.1016/1352-2310\(94\)00217-9](https://doi.org/10.1016/1352-2310(94)00217-9)
- 845 Mahrt, L. (2010). Variability and Maintenance of Turbulence in the Very Stable  
846 Boundary Layer. *Boundary-Layer Meteorology*, 135(1), 1–18.  
847 <https://doi.org/10.1007/s10546-009-9463-6>
- 848 Mahrt, L., & Bou-Zeid, E. (2020). Non-stationary Boundary Layers. *Boundary-Layer*  
849 *Meteorology*. <https://doi.org/10.1007/s10546-020-00533-w>
- 850 Mazon, J., & Pino, D. (2015). Role of the nocturnal coastal-front depth on cloud  
851 formation and precipitation in the Mediterranean basin. *Atmospheric Research*, 153,  
852 145–154. <https://doi.org/10.1016/j.atmosres.2014.08.004>
- 853 Mitsumoto, S., Ueda, H., & Ozoe, H. (1983). A Laboratory Experiment on the Dynamics  
854 of the Land and Sea Breeze. *Journal of the Atmospheric Sciences*, 40(5), 1228–  
855 1240. [https://doi.org/10.1175/1520-0469\(1983\)040<1228:ALEOTD>2.0.CO;2](https://doi.org/10.1175/1520-0469(1983)040<1228:ALEOTD>2.0.CO;2)
- 856 Moroni, M., & Cenedese, A. (2015). Laboratory Simulations of Local Winds in the  
857 Atmospheric Boundary Layer via Image Analysis. *Advances in Meteorology*, 2015,  
858 1–34. <https://doi.org/10.1155/2015/618903>

- 859 Pope, S. B. (2001). Turbulent Flows. *Measurement Science and Technology*.  
860 <https://doi.org/10.1088/0957-0233/12/11/705>
- 861 Porson, A., Steyn, D. G., & Schayes, G. (2007). Sea-breeze scaling from numerical  
862 model simulations, Part I: Pure sea breezes. *Boundary-Layer Meteorology*.  
863 <https://doi.org/10.1007/s10546-006-9090-4>
- 864 Porté-Agel, F., Bastankhah, M., & Shamsoddin, S. (2020). Wind-Turbine and Wind-  
865 Farm Flows: A Review. *Boundary-Layer Meteorology*, 174(1), 1–59.  
866 <https://doi.org/10.1007/s10546-019-00473-0>
- 867 Richter-Menge, J., Overland, J. E., Mathis, J. T., & Osborne, E. (2017). *Arctic Report*  
868 *Card 2017*. 1–96.
- 869 Rizza, U., Miglietta, M. M., Anabor, V., Degrazia, G. A., & Maldaner, S. (2015). Large-  
870 eddy simulation of sea breeze at an idealized peninsular site. *Journal of Marine*  
871 *Systems*, 148, 167–182. <https://doi.org/10.1016/j.jmarsys.2015.03.001>
- 872 Salesky, S. T., Chamecki, M., & Bou-Zeid, E. (2017). On the Nature of the Transition  
873 Between Roll and Cellular Organization in the Convective Boundary Layer.  
874 *Boundary-Layer Meteorology*. <https://doi.org/10.1007/s10546-016-0220-3>
- 875 Segal, M., Leuthold, M., Arritt, R. W., Andersen, C., & Shen, J. (1997). Small Lake  
876 Daytime Breezes: Some Observational and Conceptual Evaluations. *Bulletin of the*  
877 *American Meteorological Society*. [https://doi.org/10.1175/1520-](https://doi.org/10.1175/1520-0477(1997)078<1135:SLDBSO>2.0.CO;2)  
878 [0477\(1997\)078<1135:SLDBSO>2.0.CO;2](https://doi.org/10.1175/1520-0477(1997)078<1135:SLDBSO>2.0.CO;2)
- 879 Sha, W., Kawamura, T., & Ueda, H. (1991). A Numerical Study on Sea/Land Breezes as  
880 a Gravity Current: Kelvin–Helmholtz Billows and Inland Penetration of the Sea-  
881 Breeze Front. *Journal of the Atmospheric Sciences*, 48(14), 1649–1665.  
882 [https://doi.org/10.1175/1520-0469\(1991\)048<1649:ANSOSB>2.0.CO;2](https://doi.org/10.1175/1520-0469(1991)048<1649:ANSOSB>2.0.CO;2)
- 883 Sills, D. M. L., Brook, J. R., Levy, I., Makar, P. A., Zhang, J., & Taylor, P. A. (2011).  
884 Lake breezes in the southern Great Lakes region and their influence during BAQS-  
885 Met 2007. *Atmospheric Chemistry and Physics*. [https://doi.org/10.5194/acp-11-](https://doi.org/10.5194/acp-11-7955-2011)  
886 [7955-2011](https://doi.org/10.5194/acp-11-7955-2011)
- 887 Spalart, P. R. (1988). Direct simulation of a turbulent boundary layer up to  $R_0 = 1410$ .  
888 *Journal of Fluid Mechanics*. <https://doi.org/10.1017/S0022112088000345>

- 889 Steyn, D. G. (2003). Scaling the vertical structure of sea breezes revisited. *Boundary-*  
890 *Layer Meteorology*. <https://doi.org/10.1023/A:1021568117280>
- 891 van der Wiel, K., Gille, S. T., Llewellyn Smith, S. G., Linden, P. F., & Cenedese, C.  
892 (2017). Characteristics of colliding sea breeze gravity current fronts: a laboratory  
893 study. *Quarterly Journal of the Royal Meteorological Society*, 143(704), 1434–  
894 1441. <https://doi.org/10.1002/qj.3015>
- 895 Yang, X. (1991). A study of nonhydrostatic effects in idealized sea breeze systems.  
896 *Boundary-Layer Meteorology*. <https://doi.org/10.1007/BF00119419>  
897



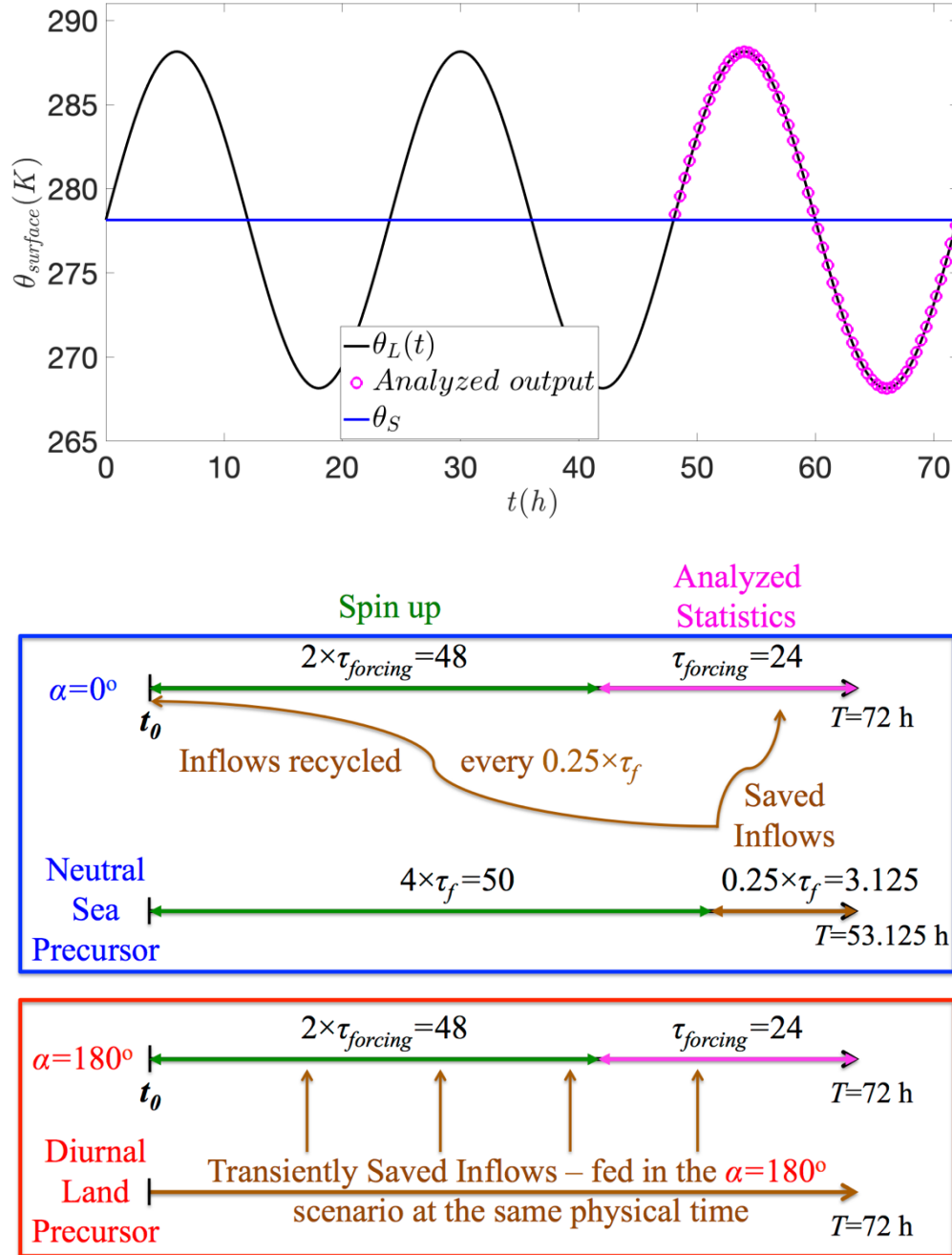
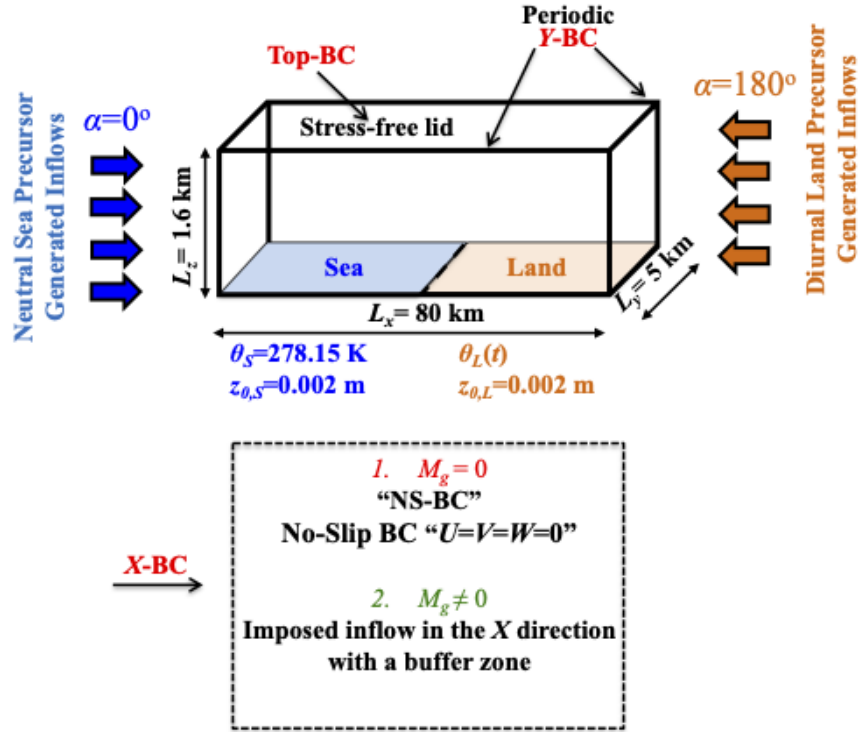


Fig. 1 The simulated diurnal surface temperature profile over the two patches. “Analyzed results” correspond to the third 24 hours period (top panel). Schematic of spin-up, inflows, and analyses periods for the  $\alpha=0^\circ$  and  $\alpha=180^\circ$  simulations (bottom panel)



903  
904 Fig. 2 Three dimensional schematic diagram of the sea-land heterogeneous simulation, BCs are fully  
905 detailed in ABI23  
906

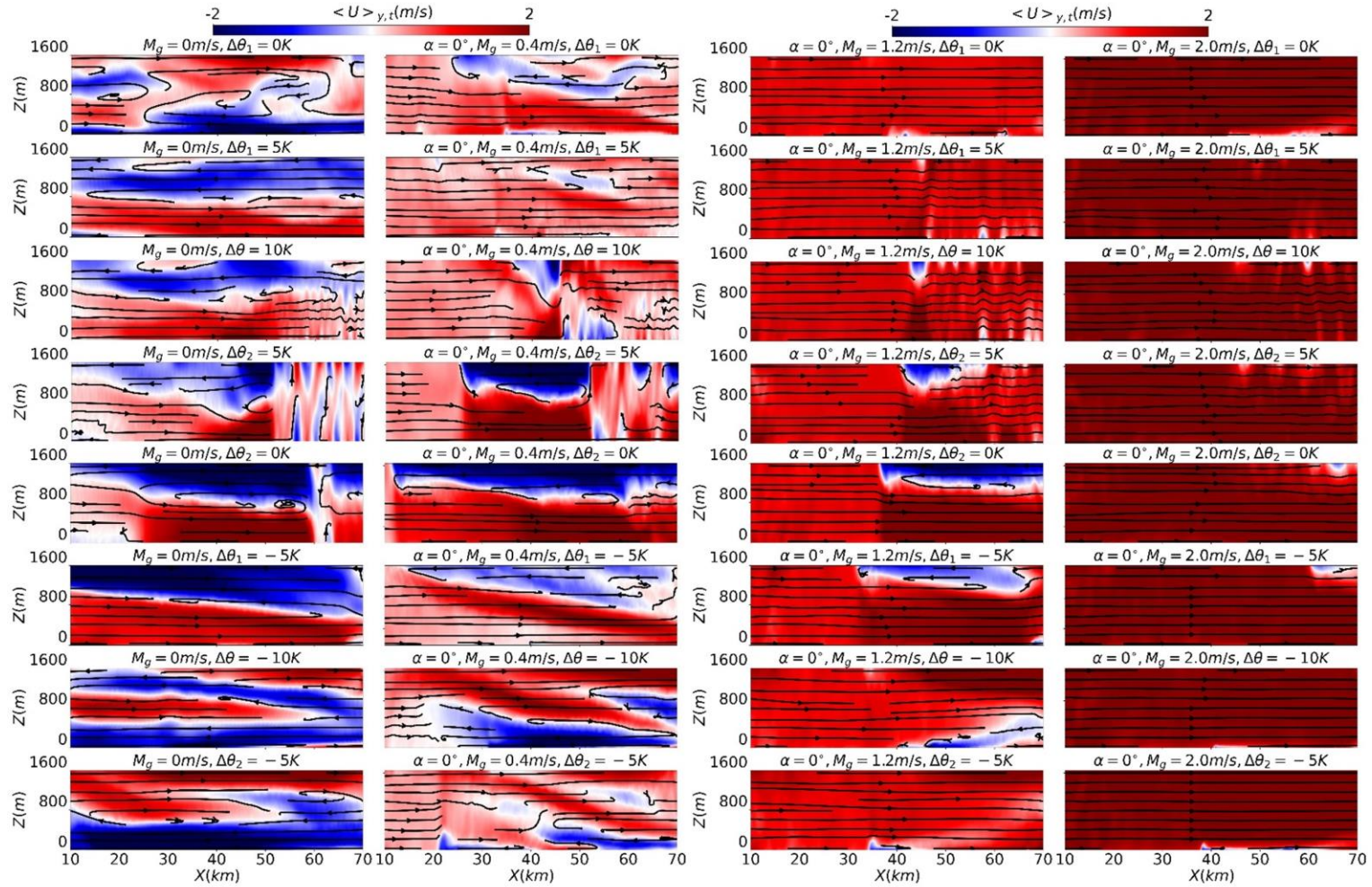
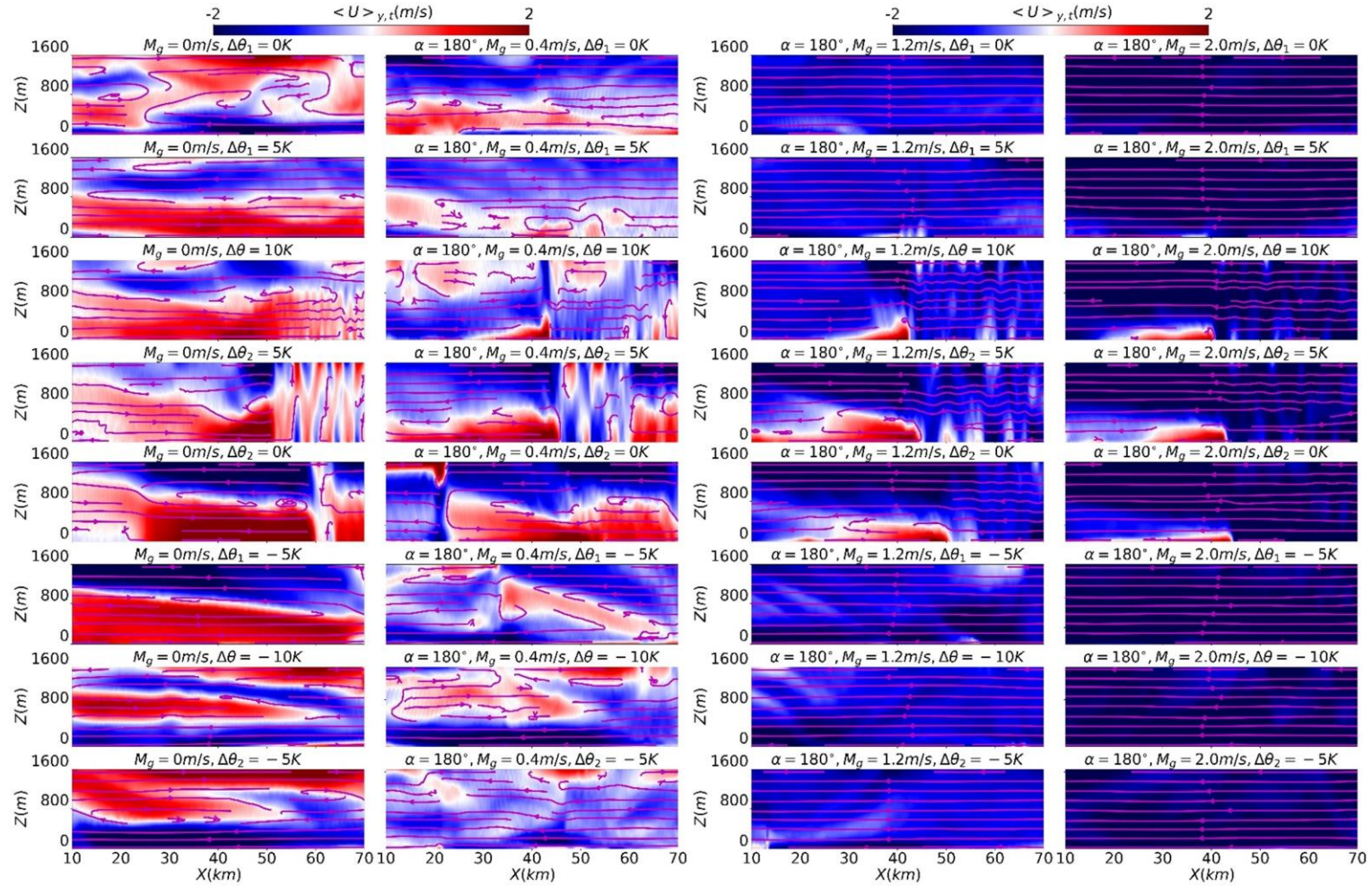


Fig. 3 Pseudocolor plots of along shore, time averaged stream-wise velocity  $\langle U \rangle_{y,t}$  through an X-Z slice of the analysis domain.

The panels here correspond to  $\alpha = 0^\circ$





910

911 Fig. 4 Pseudocolor plots of along shore, time averaged stream-wise velocity  $\langle U \rangle_{y,t}$  through an X-Z slice of the analysis domain.

912 The panels here correspond to  $\alpha=180^\circ$

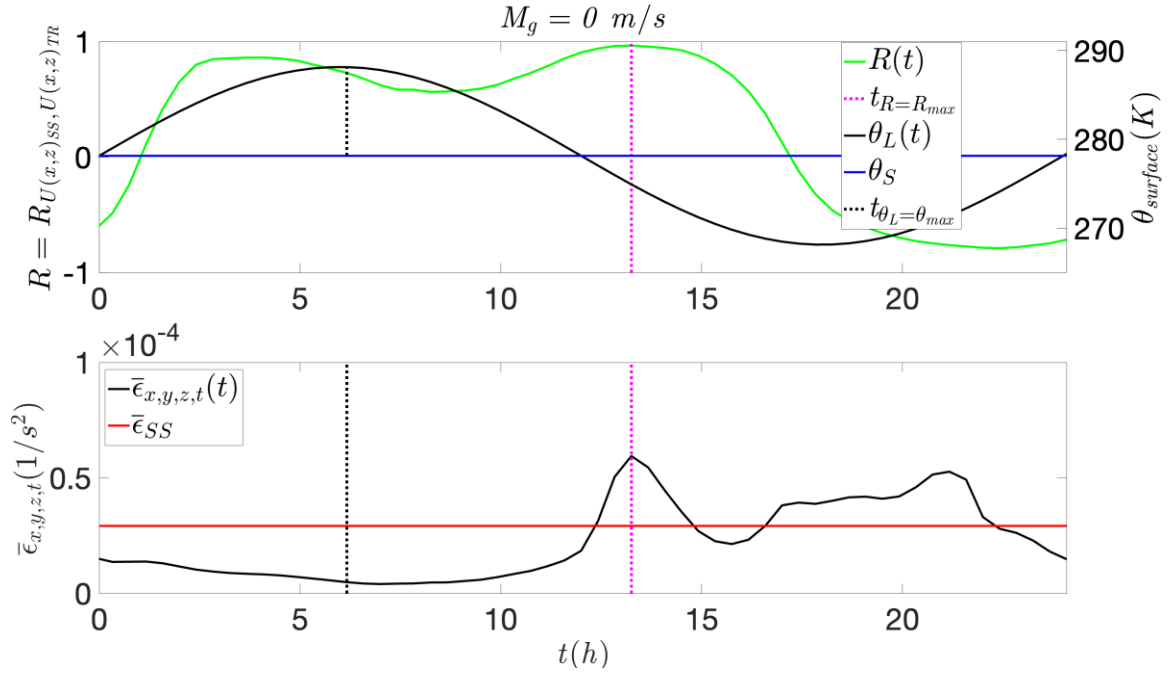


Fig. 5 The correlation coefficient transient behavior of  $\langle U \rangle_{x,z}$  “subscripts: SS refers to one steady state snapshot when  $\theta_L = \theta_{max}$ , and TR refers to the transient snapshots of the unsteady simulation” for  $M_g=0$  (top panel). The corresponding averaged enstrophy is shown here (bottom panel)

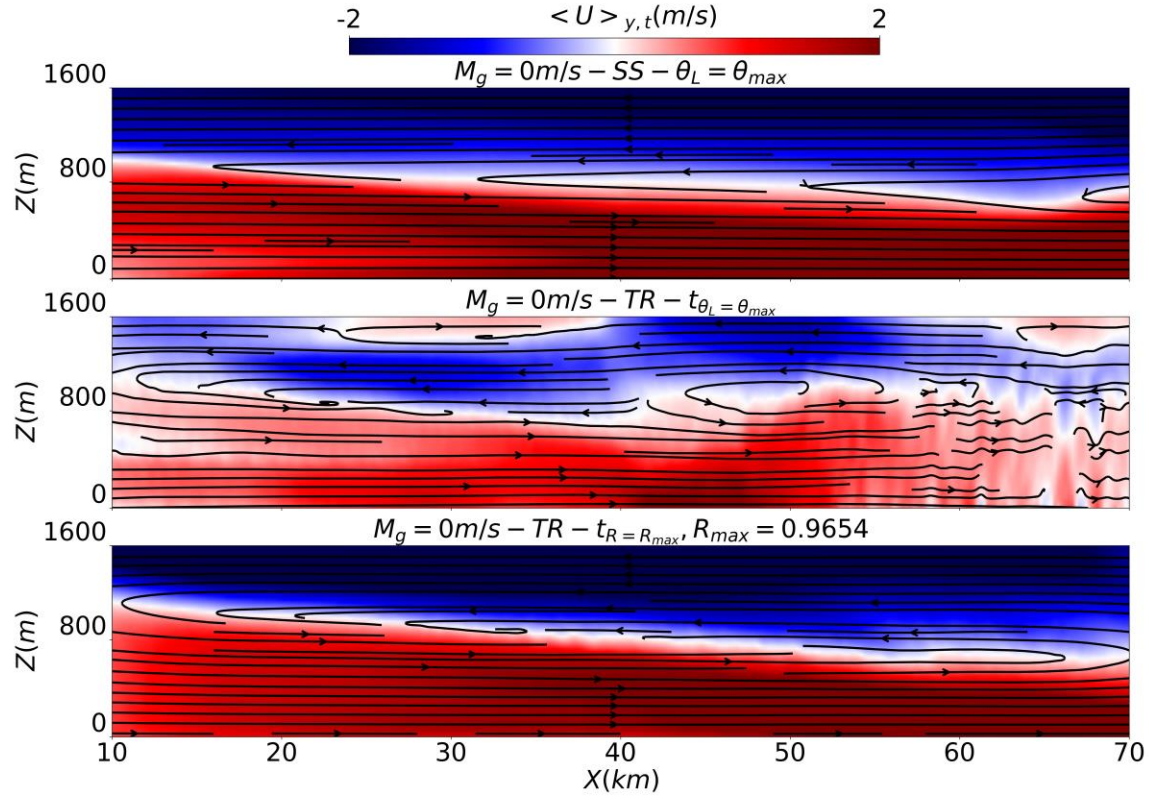


Fig. 6 The corresponding snapshots of  $\langle U \rangle_{x,z}$  “SS:  $\theta_L = \theta_{max}$ ” (top), “TR:  $t_{\theta_L} = \theta_{max}$ ” (middle), and “TR:  $t_R = R_{max}$ ” (bottom) for  $M_g = 0$

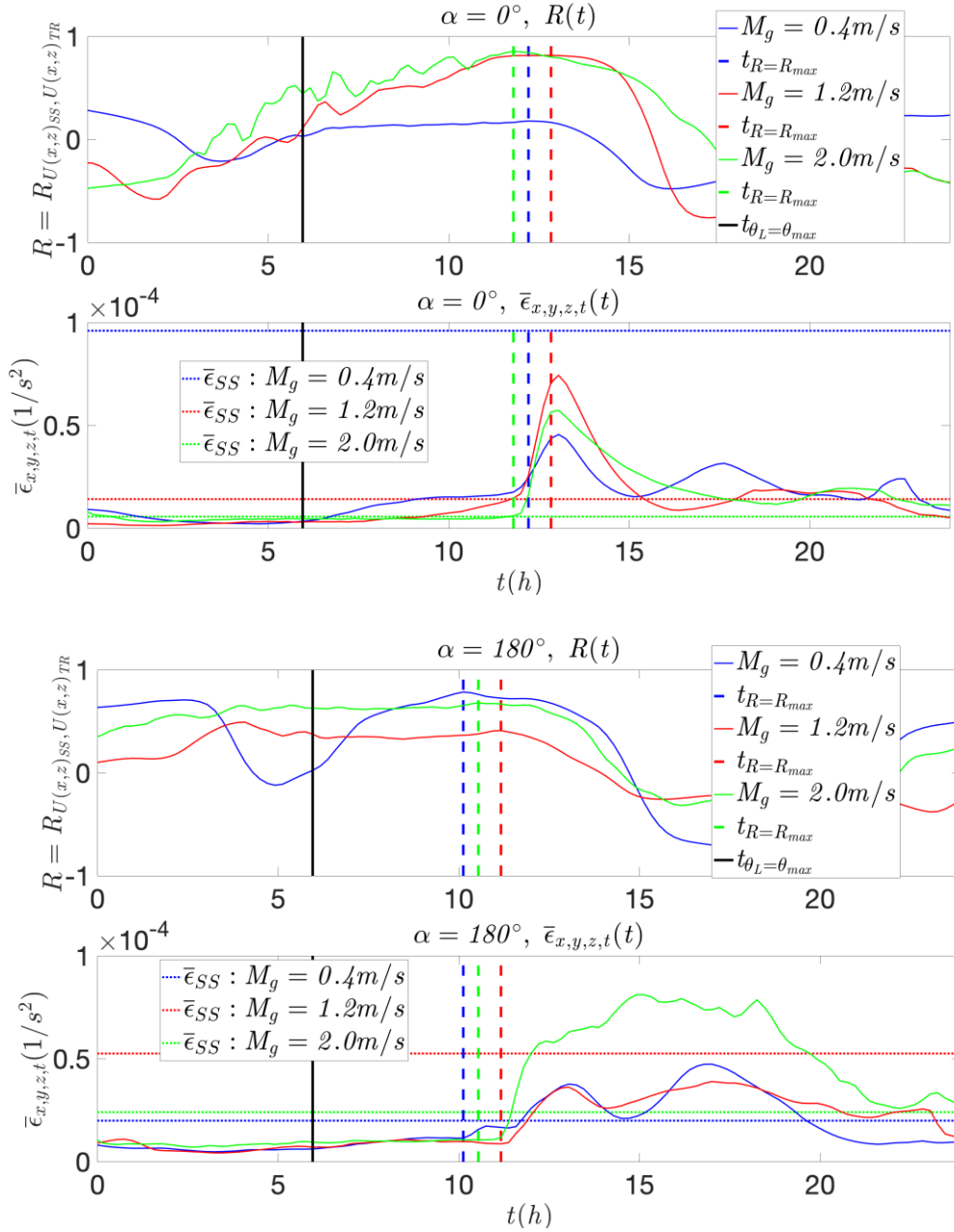


Fig. 7 The correlation coefficient transient behavior of  $\langle U \rangle_{x,z}$  and the corresponding averaged enstrophy for  $\alpha=0^\circ$  (top panel). Similarly, for  $\alpha=180^\circ$  (bottom panel)

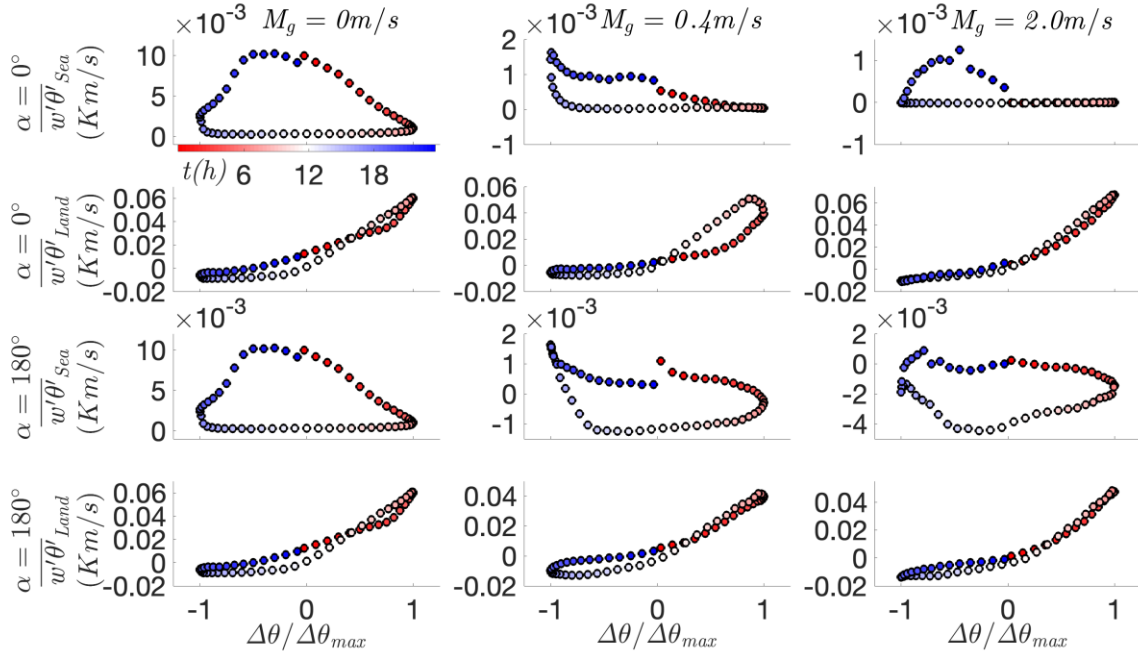


Fig. 8 The diurnal behavior of surface heat fluxes over the sea and land patches respectively with increasing  $M_g$  along  $\alpha=0^\circ$  (top two rows). Similarly, for  $\alpha=180^\circ$  (bottom two rows)



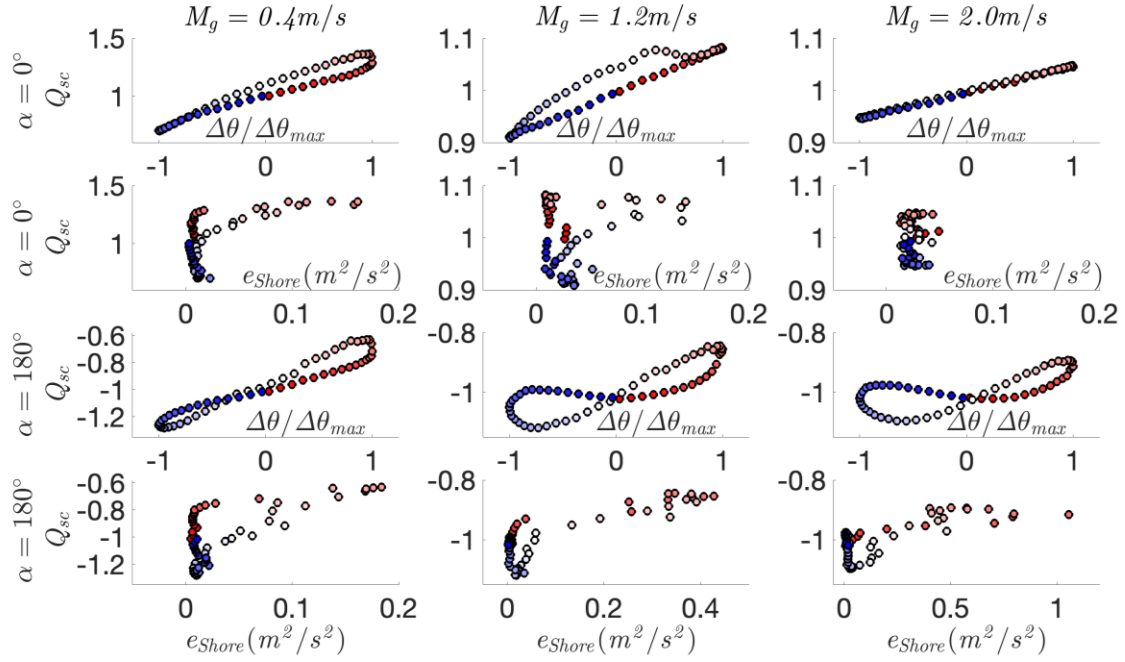


Fig. 9 The diurnal behavior of the normalized net shore volumetric flux ( $Q_{sc}$ ) relative to the imposed forcing  $\Delta\theta$  and TKE,  $e_{Shore}$ , with increasing  $M_g$  along  $\alpha=0^\circ$  (top two rows). Similarly, for  $\alpha=180^\circ$  (bottom two rows).

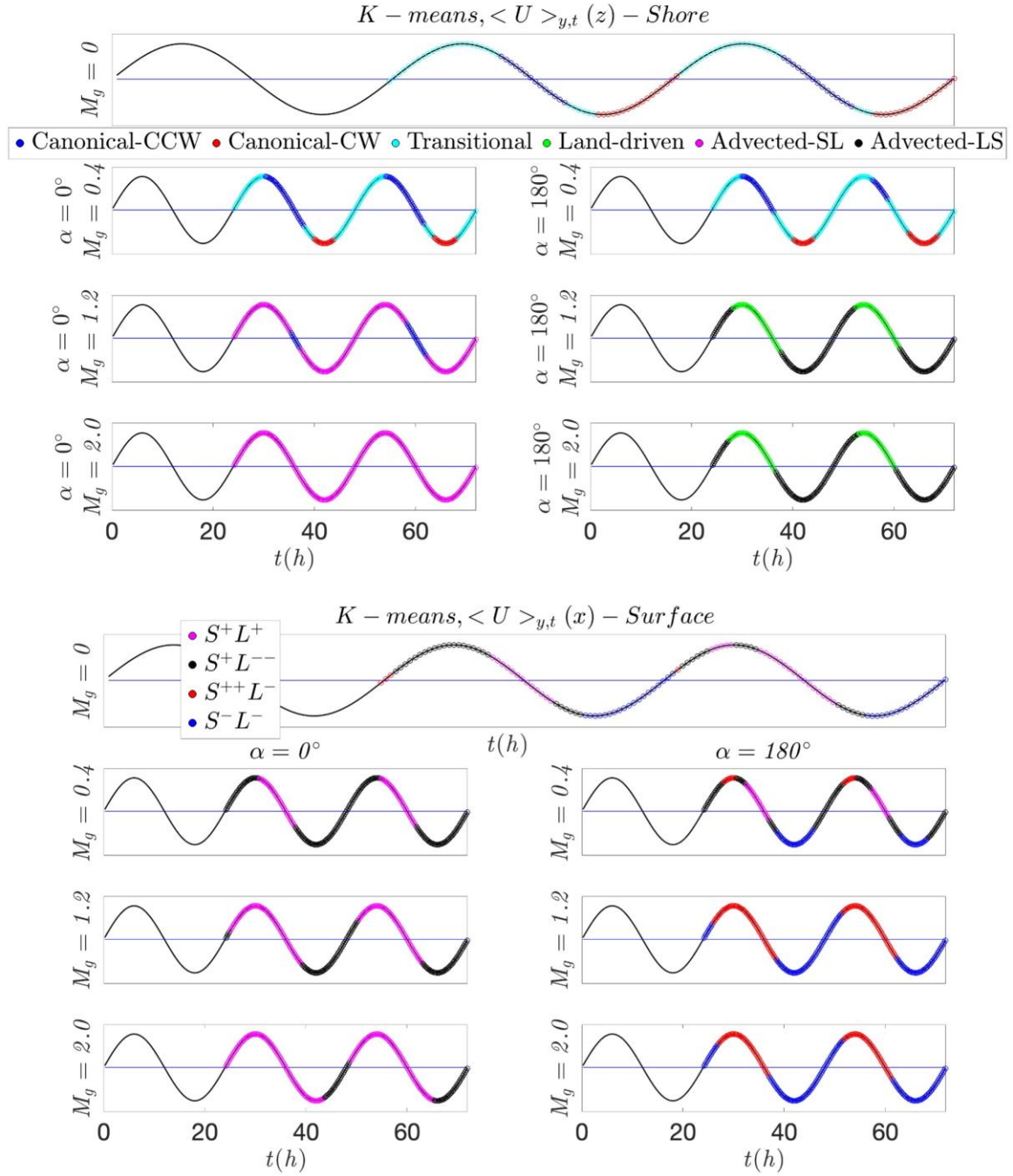


Fig. 10 Macro classification of all the transient simulations using the  $k$ -means algorithm with  $U(z)_{shore}$  (top). Micro classification with  $U(x)$  - surface (bottom)